# The 2015–2017 Pamir Earthquake Sequence: Fore-, Main-, and Aftershocks, Seismotectonics, Fault Interaction, and Fluid Processes

**Wasja Bloch[1*], Sabrina Metzger[1], Bernd Schurr[1], Xiaohui Yuan[1], Lothar Ratschbacher[2], Sanaa Reuter[2], Qiang Xu[3,4], Junmeng Zhao[3,4], Shokhruhk Murodkulov[5], Ilhomjon Oimuhammadzoda[6]**

[1]GFZ German Research Centre for Geosciences, 14473 Potsdam, Germany

[2]Geologie, Technische Universität Bergakademie Freiberg, 09599 Freiberg, Germany

[3]Key Laboratory of Continental Collision and Plateau Uplift, Institute of Tibetan Plateau Research, Chinese Academy of Sciences, Beijing 100101, China

[4]CAS Center for Excellence in Tibetan Plateau Earth Sciences, Beijing 100101, China

[5]Institute of Geology, Earthquake Engineering and Seismology, National Academy of Sciences, Dushanbe, Tajikistan

[6]Department of Geology under the Government of the Republic of Tajikistan, Dushanbe, Tajikistan

**Key Points:**

- New Pamir earthquake and moment tensor catalogs (2015–2017) contain numerous fore- and aftershocks.
- Identification of the major seismo-tectonically active faults in the Pamir and southern Tian Shan
- Subordinate role of stress transfer in the triggering of large earthquakes, but indications for earthquake-activated fluid processes

*Now at: Department of Earth, Ocean and Atmospheric Sciences, University of British Columbia

Corresponding author: Wasja Bloch, wbloch@eoas.ubc.ca

## Abstract

A sequence of three strong ($M_W$7.2, 6.4, 6.6) earthquakes struck the Pamir of Central Asia in 2015–2017. With a local seismic network we recorded the succession of the fore-, main-, and aftershock sequences at local distances with good azimuthal coverage. We located 11,784 seismic events and determined 33 earthquake moment tensors. The seismicity delineates the major tectonic structures of the Pamir, i.e., the thrusts that absorb shortening along the Pamir's thrust front, and the strike-slip and normal faults that dissect the Pamir Plateau into a westward extruding block and a northward advancing block. Fault ruptures were activated subsequently from the initial $M_W$7.2 Sarez event at times and distances that follow a diffusion equation. All mainshock areas but the initial one exhibited foreshock activity which was not modulated by the occurrence of the earlier earthquakes. Modeling of the static Coulomb stress changes indicates that aftershock triggering occurred over distances of $\leq$90 km on favorably oriented faults. The 3rd event in the sequence, the $M_W$6.6 Muji earthquake, ruptured despite its repeated stabilization through stress transfer in the order of -10 kPa. To explain the significant accumulation of $M_W > 6$ earthquakes, we reason that the initial mainshock may have increased nearby fault permeability, and facilitated fluid migration into the mature fault zones, eventually triggering the later large earthquakes.



## Plain Language Summary

A sequence of strong and moderate earthquakes occurred in the Pamir of Central Asia between 2015 and 2017. We had a dense network of seismometers in operation, which recorded the earthquakes from close distance. In total, we located 11,784 earthquakes that occurred before and after three major ones. Of 33 earthquakes, we could determine their rupture-plane orientation. Our dataset traces the tectonic structures along which the Pamir deforms. The Pamir is growing outwards and is dissected in the middle. The three largest earthquakes occurred at successively greater distances from the first one and all but the first large earthquake were preceded by many smaller ones. The stress that the earlier earthquakes exerted on the later ones is significant only at rather small distances. For more distant earthquakes, stress changes were small or even negative. The transferred stresses cannot explain why so many strong earthquakes occurred in sequence. We find indications that fluids inside the upper crust were freed by the first earthquake,

which then migrated through the damage zones and may have triggered some of the later large earthquakes.

## 1 Introduction

The Pamir occupies the northwestern tip of the India-Asia collision zone, where several major mountain belts—the Tian Shan, Kunlun Shan, Karakorum, and Hindu Kush—and two large depressions—the Tarim and Afghan-Tajik basins—converge (Figure 1). The Pamir represents Asian lithosphere far north of the Indus-Yarlung suture zone that separates Indian from Asian crust. Nonetheless, it exhibits some of the highest strain rates for an intra-continental setting, both within the broad India-Asia collision zone and globally (Kreemer et al., 2014). Deformation involves shortening and dextral strike-slip shear along its northern margin and sinistral strike-slip faulting and extension in its interior, the Pamir Plateau (Schurr et al., 2014). Between December 2015 and November 2016, one moment magnitude $M_W$7 and two $M_W$6+ earthquakes hit the Pamir Plateau and its northern margin, activating a major fault network. The sequence started with the December 7, 2015 $M_W$7.2 Sarez sinistral strike-slip earthquake, which ruptured three segments of the Sarez-Karakul Fault System (SKFS) with a total length of ∼80 km (Figure 1a; Sangha et al., 2017; Metzger et al., 2017; Elliott et al., 2020). About 6 months later, the June 26, 2016 $M_W$6.4 Sary-Tash earthquake ruptured a reverse fault, probably in the Tian Shan basement below the Main Pamir Thrust System (MPTS; see section 4.3.; He et al., 2018), ∼90 km NNE of the northern end of the Sarez rupture. Another 5 months later, the November 25, 2016 $M_W$6.6 Muji earthquake broke two segments of the Muji Fault (Bie et al., 2018; T. Li et al., 2019; J. Li et al., 2019), ∼30 km SW of the Sary-Tash earthquake (Figure 1a). Even for a region as seismically-active as the Pamir, this sequence was unusual: Long-term earthquake bulletins (e.g., the Global Earthquake Model ISC-GEM; Di Giacomo et al., 2018; ISC, 2021) report only 18 $M_W > 6.5$ earthquakes in the region between 1900 and 2015 (Figure 1b). The probability that the three recent $M_W > 6.4$ earthquakes occurred independent of each other, i.e., following a Poisson process, is 0.05%.

After a large earthquake, aftershocks occur in the volume where the stresses were increased (Toda et al., 1998; Stein, 1999; Ryder et al., 2012; Toda & Stein, 2020). Sometimes, they trigger large mainshocks in cascades which will then become foreshocks (Ellsworth & Bulut, 2018; Chen et al., 2020; Schurr et al., 2020). Triggering may be delayed if receiving fault friction parameters are dependent on slip-rate and -state (e.g. Dieterich,

1992), or if the crust or upper mantle relaxes viscously (e.g., Freed & Lin, 2001). An increase in pore-pressure through deformation or migrating fluids may account for complex spatio-temporal seismicity patterns (e.g. Miller, 2020; Yamashita, 1999). In the present case, the earthquakes occurred on kinematically dissimilar fault zones and over comparatively large distances. Transferred stresses acted highly oblique or opposed to the slip directions of the receiving faults (Figure 2), leaving the mechanism of earthquake interaction unclear.

Since August 2015, we had a temporary seismic network in operation in the eastern Pamir in the Xinjiang province of China. It recorded the initial December 2015 Sarez earthquake (Figure 1a). In February 2016, we deployed a network on the Pamir Plateau of Tajikistan in the vicinity of the Sarez earthquake rupture. The combined networks recorded then both the June 2016 Sary-Tash and the November 2016 Muji earthquake sequences with a very good azimuthal coverage. Additional moderate earthquakes with their own fore- and aftershock sequences augmented the recordings. The overall sequence of events allowed us to investigate the location, orientation, kinematics, and activation time of the seismically active faults in the region. These provide insight in the partitioning of deformation in the Pamir and allow studying the dynamics of fault interaction. In addition, we derived displacement rates from interferometric synthetic-aperture radar (InSAR) data to detect aseismic deformation transients. We examined the spatio-temporal seismic activation patterns to investigate earthquake interaction and nucleation. To identify longer term seismicity patterns, we compare our findings with the results of an earlier experiment (Schurr et al., 2014; Sippl et al., 2014).

## 2 Neotectonic Framework

In the Pamir, northward displacement at rates of 13–19 mm/yr is currently accommodated along its margins by crustal shortening along the MPTS in the north, in particular the Pamir Frontal Thrust (PFT), the sinistral Darvaz Fault Zone in the west and northwest, the dextral Karakorum Fault System in the southeast, and the Kongur Shan-Taxkorgan Normal Fault System in the Chinese eastern Pamir (Figure 1; e.g., Chevalier et al., 2015; Ischuk et al., 2013; Jade et al., 2004; Metzger et al., 2020; Schurr et al., 2014; Zubovich et al., 2010, 2016). The Karakorum Fault System probably links with the Sarez-Murghab Thrust System via the Aksu-Murghab Fault Zone on the Pamir Plateau (Robinson, 2009; Rutte et al., 2017). The dextral transpressive Kashgar-Yecheng Fault

System (Cowgill, 2009) linked shortening in the western Kunlun Shan and along the MPTS; since ∼5 Ma (Sobel et al., 2011) and up to now (Zubovich et al., 2010), the Pamir and the Tarim basin have been moving north at about the same rate, rendering the transform component mostly inactive. The Muji Fault links ∼E-W extension along the Kongur Shan Normal Fault System to the MPTS (T. Li et al., 2019; Schurr et al., 2014; Sippl et al., 2014). The Kongur Shan Normal Fault System has accommodated ≥35 km of ∼E-W extension, mostly since ∼7 Ma (Robinson et al., 2004, 2007; Thiede et al., 2013); extension and dextral strike-slip along the Muji Fault are ongoing, as implied by seismicity and the divergence of the Global Navigation Satellite System (GNSS) velocity field between Pamir's interior and the Tarim block (T. Li et al., 2019; Zubovich et al., 2010).

In the interior of the Pamir, the active displacement field is composed of bulk northward movement combined with ∼E-W extension (Zhou et al., 2016; Ischuk et al., 2013). The crust hosts both sinistral strike-slip faulting on ∼NE-striking or conjugate planes and—to a lesser degree—normal faulting on ∼N-striking planes (Schurr et al., 2014). In the interior of the eastern Pamir, the lack of both, thrusting and significant seismicity, demonstrate that it is moving northward en bloc; this agrees with the GNSS data. The only ∼NE-striking sinistral-transtensive fault system of the Pamir interior, which has a clear morphologic expression and is seismically active, is the SKFS. It stretches from south of Lake Sarez to north of Lake Karakul (Elliott et al., 2020; Metzger et al., 2017; Schurr et al., 2014; Strecker et al., 1995). The northern SKFS is interpreted as a horst-graben structure (Nöth, 1932; Strecker et al., 1995), the southern SKFS currently shows dominant sinistral strike-slip and subordinate normal displacements (Elliott et al., 2020; Metzger et al., 2017). The ∼E-W extension—increasing into the western Pamir—is driven by westward gravitational collapse of thickened Pamir-Plateau crust into the Tajik Depression (Metzger et al., 2020; Schurr et al., 2014; Stübner et al., 2013).

Beneath the Pamir, Asian lithosphere forms a ∼90° arc that is retreating northward and westward as traced by intermediate-depth seismicity (60–300 km; Schneider et al., 2013; Sippl, Schurr, Tympel, et al., 2013). Kufner et al. (2016) and Bloch et al. (2021) inferred that the Asian slab retreat is forced by indentation of Indian lithosphere, bulldozing into the lithosphere of the Tajik-Tarim basin at mantle depth. In this context, the SKFS and the two largest earthquakes in the Pamir interior—the December 2015 and the 1911 $M_W \sim 7.3$ (Figure 1b; Kulikova et al., 2016; Elliott et al., 2020) earthquakes—with similar sinistral strike-slip mechanisms in about the same region, likely express the

150 underthrusting of the northwestern leading edge of the Indian mantle lithosphere inden-
151 ter. The 2015 Sarez rupture may be the most recent manifestation of the shear zone at
152 the northwestern tip of the indenter, building a continuous fault zone along the inden-
153 ter's western edge and connecting the distributed sinistral fault zones of the Hindu Kush
154 with the SKFS (Kufner et al., 2018, 2021; Metzger et al., 2017; Schurr et al., 2014).

155 # 3 Data and Methods

156 ## 3.1 Seismic Data

157 We operated the East Pamir seismic network (FDSN code 8H; Yuan, Schurr, Bloch,
158 et al., 2018) with 30 sites in the eastern Pamir, northwestern Kunlun, and northwest-
159 ern Tarim Basin between August 2015 and July 2017, and the Sarez-Pamir aftershock
160 seismic network (FDSN code 9H; Yuan, Schurr, Kufner, & Bloch, 2018) with 10 sites on
161 the Pamir Plateau between February 2016 and July 2017 (Figure 1a). We used additional
162 seismic waveform data from the Xinjiang regional seismic network (SEISDMC, 2021) and
163 the Tajik National Seismic Network (FDSN code TJ; PMP International (Tajikistan),
164 2005).

165 We detected 39,309 seismic events using the *Lassie* earthquake detector as coher-
166 ent peaks in move-out corrected, smoothed, pulse-like seismogram image functions that
167 were stacked on a rectangular grid of 100×100×10 trial subsurface points with a spac-
168 ing of 10×10×30 km (Comino et al., 2017) using the 1-D velocity model of Sippl, Schurr,
169 Yuan, et al. (2013). The initial location and predicted P- and S-wave arrival times were
170 used as a starting point for phase arrival time picking. We picked P-wave arrival times
171 automatically with *MannekenPix* (Aldersons, 2004), where *obspy*'s STA/LTA triggers
172 and predicted arrivals from the detection routine were used as starting points; S-wave
173 arrival times were picked with *spicker* (Diehl et al., 2009). Filter window lengths and
174 positions for both algorithms were calibrated with manually picked phase arrivals of 59
175 events. After each picking run, events were located with *hypo71* (Lee & Lahr, 1972), and
176 arrival times with the highest residuals were removed until the location root-mean-square
177 (RMS) misfit fell below a threshold of 2 s for P-waves and 3 s for P- and S-waves com-
178 bined. We then used a subset of 1,855 seismic events with the best constrained arrival-
179 time picks to invert for a 1-D velocity model and static station corrections using *velest*
180 (Kissling et al., 1994). We removed arrival times that yielded a residual 5 times larger

than the standard deviation of all residuals of a certain seismic phase on a certain station, resulting in preliminary locations for 29,795 events. We excluded 20 apparent high-RMS misdetections (e.g., teleseismic events or network-wide null data in the XJ network), 13,149 events with less than 6 arrival time picks, 9,366 events with an azimuthal gap larger than 270° and 810 events below 300 km depth. Some events were removed due to more than one criterion. We manually revised the picks of 82 events of special interest, such as mainshocks or major foreshocks. After this step, we successfully located 11,782 seismic events in the 3-D P-wave velocity model of Bloch et al. (2021) with *simulps* (Thurber, 1983). We computed waveform cross-correlation differential arrival times of event pairs less than 10 km apart with *obspy* (Krischer et al., 2015) and determined refined relative event locations for 3,748 events using differential P- and S-wave catalog- and cross–correlation-arrival–times in *hypoDD* (Figures S1 to S3; Waldhauser & Ellsworth, 2000). The depth of 2,352 likely shallow events could not be resolved. They are located at the surface (i.e., the top boundary of the velocity model at -3 km); their map view distribution is similar to the one of events with well-constrained depths, giving us confidence that they do not bias the overall seismicity pattern (Data Set S1).

### 3.2 Regional Moment Tensors

We determined regional moment tensors using the *RMT* algorithm of Nábělek and Xia (1995). Green's functions were computed with the discrete wavenumber summation method of Bouchon (1981) from the velocity and damping structure previously obtained by Sippl, Schurr, Yuan, et al. (2013) (Figure S4). Seismograms were band-pass filtered per event at lowest possible frequencies still providing good signal. For most events, filter corners of 20 and 60 s were suitable. Only events 2, 5, and 7 (Table 1) were filtered with a broader pass band between 15 and 80 s, and events 1, 3, and 7 with a narrower one between 10 and 40 s. Noisy waveforms were discarded interactively. We allowed small timing adjustments between observed and synthetic seismograms to match the phase. In total, we were able to retrieve 33 moment tensors of events with moment magnitude $M_W$ between 4.0 and 6.0 (Table 1, Data Set S2). Moment tensors of the three large mainshocks could not be computed due to clipped waveforms; we instead report the moment tensor and magnitude published by the National Earthquake Information Center (NEIC).

A comparison between moment tensors and magnitudes of 10 events that were also analysed by NEIC shows that the focal mechanisms agree (Figure S5a). Significant dif-

ferences occur only for two events from the Sary-Tash aftershock sequence (8 and 11 in Figure S5a). Within the context of other similar mechanisms in the sequence, the good waveform fit (Figure S6 and S7), and given our better database, we are confident in our solutions.

### 3.3 Magnitudes

Calibrated local magnitudes $M_L$ were obtained for all events by investigating the largest horizontal ground displacement amplitude $A$ as a function of distance $R$. Following Bormann and Dewey (2012), we corrected the seismograms from their respective instrument response function and convolved them with the one of a Wood-Anderson seismograph. We measured the largest amplitude of any of the horizontal components and calibrated the magnitude–amplitude–distance relationship (Bormann & Dewey, 2012):

$$M_L^i = \log_{10} A^i + B \log_{10} R^i + C R^i + D \tag{1}$$

by minimizing:

$$\epsilon = \frac{1}{N} \sum_{i=1}^{N} \sqrt{\left(M_L^i - M_W^i\right)^2} \tag{2}$$

for all 921 station observations $i$ of the 33 events for which $M_W$ is available (Figure S5c). We report the so calibrated $M_L$ as the mean value of $M_L^i$ after removal of outliers.

We computed the magnitude of completeness $M_c$ of the entire catalog as the lower end of the longest linear segment of the cumulative frequency–magnitude distribution (Figure S5d). A daily minimum completeness magnitude $M_c^{min}$ was computed as the most frequent magnitude (binned in intervals of 0.1) observed in the previous 60 days (Woessner & Wiemer, 2005).

### 3.4 InSAR Displacement and Fault Creep Model

To investigate possible creep on the SKFS, we analysed automatically generated radar interferograms (Lazecký et al., 2020) of ascending frame 100A_052 and descending frame 005D_050 (following Comet LiCS naming convention), covering the southern and northern part of the SKFS, respectively. We included all available data following the Sarez mainshock, that is 27 months for the southern frame (36 radar scenes, 93 interferograms; Figure S8), and 5 months for the northern frame (5 radar scenes, 7 interferograms, Figure S9), before they were affected by the Sary-Tash earthquake thereafter.

We therefore excluded subsequent acquisitions. After a visual data inspection and manual unwrapping error correction we calculated linear displacement rates using the small-baseline time-series analysis software *LiCSBAS* (Morishita et al., 2020). We subsampled (multi-looked) the original interferograms four times to a spatial resolution of ∼400 m, clipped them to the area of interest and subtracted the predicted atmospheric signal delay using state-of-the-art weather models (Yu et al., 2018). We applied a temporal low-pass filter of 42 days and a spatial low-pass filter of 2 km to the time-series of frame 100A_052, and no filter to frame 005D_050 (Hooper, 2008). Then we extracted linear rate maps (Figure S10).

We converted the rate maps into displacement accumulated over the 202 days between the Sarez and Sary-Tash mainshocks, assuming a constant displacement rate due to post-seismic slip within the first few months following the Sarez main shock. We modeled the observed surface displacements using vertical, rectangular dislocation sources (Okada, 1985) with uniform sinistral slip, assuming a homogeneous half space subsurface model with Lamé's parameters $\lambda = 32\,\text{GPa}$ and $G = 32\,\text{GPa}$. Source location, depth and amount of slip were modified interactively using *kite* (Isken et al., 2017) until the predicted surface displacements fitted our observations reasonably well.

### 3.5 Coulomb Stress Changes

We modeled whether the stresses induced by the large earthquakes and corresponding foreshocks loaded or unloaded nearby fault segments by computing the change in Coulomb failure stress ΔCFS (Harris, 1998):

$$\Delta CFS = \Delta\tau + \mu(\Delta\sigma_n + \Delta p). \tag{3}$$

$\Delta\tau$ is the change in shear stress on the fault (positive in slip direction), $\Delta\sigma_n$ is the change in normal stress (a positive ΔCFS acts destabilizing). For most rocks $\mu$ is between 0.6 and 0.8 (Harris, 1998). Under the assumption of undrained conditions (the pore fluids do not escape or enter the fault), $\Delta p$ is proportional to the mean stress change inside the fault (Rice & Cleary, 1976):

$$\Delta p = -\beta\frac{\Delta\sigma_{kk}}{3}, \tag{4}$$

where $\Delta\sigma_{kk}$ is the sum of the diagonal elements of the stress tensor and $\beta$ is the Skempton coefficient. $\beta$ lies between 0.5 and 1.0 for rocks, but is typically between 0.7 and 0.9 (Harris, 1998; Cocco & Rice, 2002). $\beta$ and $\mu$ are often combined into the apparent fric-

tion coefficient:

$$\mu' = \mu(1 - \beta). \tag{5}$$

We modeled the stress changes in response to the largest earthquakes, foreshocks and post-seismic slip transients using *pscmp* (Wang et al., 2006). We constructed dislocation sources (Okada, 1985) from published fault-slip models (Metzger et al., 2017; He et al., 2018; Bie et al., 2018) and our own earthquake moment tensors. The fault length $l$ and width $w$ of moment tensor sources were estimated from $M_W$ using the empirical scaling relationships of Wells and Coppersmith (1994):

$$w = 10^{(M_W - 4.06)/2.25)} \tag{6}$$

$$l = 10^{(M_W - 4.38)/1.49)}. \tag{7}$$

Slip $s$ was calculated from $M_0 = AGs$, with the seismic moment $M_0$, fault area $A$, and shear modulus $G = 32\,\mathrm{GPa}$. The slip sense was determined after resolution of the nodal plane ambiguity (Section 5). We then computed $\Delta$CFS according to Equations (3) and (4) at the origin times and on the fault planes of the three large earthquakes and significant foreshocks. We used an elastic half space subsurface model with Lamé's parameters $\lambda = 32\,\mathrm{GPa}$ and $G = 32\,\mathrm{GPa}$ and chose $\mu = 0.8$ and $\beta = 0.75$, so that the earthquake hypocenters received the largest $\Delta$CFS concentration while the parameters remained in the physically plausible range. We tested $\mu = 0.4$ and $\beta = 0.5$ as well as the debated assumption that $\Delta p = 0$ (Harris, 1998) by letting $\beta = 0$ and $\mu = \mu' = 0.2$. We found uncertainties in $\Delta$CFS by randomly perturbing the modeling parameters using a normal distribution. The half space parameters $\lambda$ and $G$ were varied with a standard deviation of $5\,\mathrm{GPa}$; the fault properties $\mu$ and $\beta$ with one of 0.2 (assuring they remained in the [0, 1] range); and the fault's strike, dip, and rake with one of 5°. We report the median, and the 5% and 95% quantiles of the resulting distributions (Table 1, Figure S11 and S12).

## 4 Spatio-temporal Evolution of Seismicity

Figure 3 shows different representations of the spatio-temporal seismicity pattern. In the following, regions of distinct seismic activity are denoted with capital letters *A*–*I*. They are defined as rectangular areas around the three largest mainshock fault zones (*A*, *C*, *E*) and 15 km radii around the more moderate mainshocks (*B*, *D*, *F*–*I*) down to 50 km depth (Figure 3a). The largest earthquake within each volume, specifically its hypocen-

tral location and time, is denoted with an asterisk ($A^*$–$I^*$). Foreshocks are events that occurred in the so-defined volumes before the respective mainshock.

Seismicity in the studied time period was high and modulated by the occurrence of the three major earthquakes, which mark peaks in the detected earthquake rate (Figures 3b and 3c) at an overall magnitude of completeness $M_c = 2.3$ (Figure S5d). The Sarez mainshock $A^*$ and early aftershocks occurred when only the 8H seismic network was in operation. Hence, the magnitude of completeness was relatively high in the mainshock area ($M_c^{min} \approx 2.5$, Figure 3d), compared to the eastern Pamir and Tarim basin area ($M_c^{min} \approx 1.6 - 2$). The installation of the 9H network in February 2016 on the Pamir Plateau increased the sensitivity of the entire network significantly ($M_c^{min} \approx 1.8$), even though high aftershock productivity deteriorated the detection threshold at times ($M_c^{min} \approx 2.2$). Other peaks in the event rate are due to the largest aftershock of the Sarez earthquake ($B^*$), an earthquake swarm in the western Pamir ($D$), and $M_W$4–5 earthquakes near Yarkant ($F^*$), Khorog ($G^*$), Karamyk ($H^*$), and Taxkorgan ($I^*$; Figures 3a and 3c; Table 1).

The mainshocks $B^*$–$H^*$, following the Sarez earthquake, sequentially activated fault zones at increasing Euclidean epicentral distance $r$ from the centroid location of the Sarez earthquake (Figure 3e). The time of the fault activation is approximately enclosed in an envelope function of the form of a diffusion equation (Shapiro et al., 2003, 1997):

$$r = r_0 + \sqrt{2\pi D(t - t_0)}, \tag{8}$$

where $r_0$ is the distance from the Sarez centroid to the northern or southern end of the rupture, $t_0$ is the main shock origin time (Table 1) and $D$ is a scaling constant that may be interpreted as hydraulic diffusivity. For seismicity north of the Sarez earthquake, $D$ can be estimated between 30 $m^2/s$, when enclosing the later mainshock hypocenters, and 40 $m^2/s$, when enclosing their entire rupture planes (marked by the aftershock seismicity); south of the earthquake $D$ can be estimated by the same means between 12 and 20 $m^2/s$, respectively. The sequential activation is not observed in the foreshock activity (Figures 3c and 3e). The fault volumes $A$, $B$, $C$, $D$, $E$, and $G$ were seismically active before the respective mainshocks—even years before, as recorded by the local TIPAGE seismic network (Schurr et al., 2014). This makes the distinction between foreshocks and background seismic activity only possible in retrospect. It is also not evident that the foreshock activity was triggered, enhanced, or diminished by any mainshock. Some rup-

ture volumes showed phases of increased foreshock activity ($C$ in February and April 2016, $E$ in May and August 2016; Figure 3c) and aftershock rates ($C$ in August 2016, $E$ in February 2017; Figure S13). However, they do not correlate regionally, but rather represent subordinate aftershock sequences. Only volume $B$ of the largest Sarez aftershock, which occurred ∼25 km from the Sarez epicenter, started to become seismically active immediately after the Sarez mainshock.

Crustal seismicity that is not associated with any of the mainshocks delineates known neotectonic structures (Figures 1 and 3a): the MPTS exhibited diffuse seismic activity; the Kongur Shan Normal Fault System was seismically active between the Muji Fault and the northern end of the Taxkorgan Fault; and so was a swath along the Aksu-Murghab Fault Zone in the south-central Pamir. In the following, we investigate the mainshock volumes in detail.

## 5 Seismotectonics of the mainshocks

### 5.1 Sarez Earthquake

The 2015 $M_W$7.2 Sarez earthquake ($A*$ in Figures 3, 4, and 5; Table 1) ruptured an ∼80 km long part of the SKFS between Lake Sarez and the Kokujbel Valley south of Lake Karakul (Elliott et al., 2020; Metzger et al., 2017; Sangha et al., 2017). Metzger et al. (2017) divided the rupture plane into three segments distinguished by strike changes (Figure 4a). The northern part of the southern segment showed swarm-like seismic activity with 290 events detected during the August 2008 to July 2010 TIPAGE deployment (Figure 4b; Sippl, Schurr, Yuan, et al., 2013). The swarm had ceased in August 2015, with only one $M_L$2.4 event detected on the fault in the 4 months before the Sarez mainshock (Figure 4b, ∼20 km from the hypocenter). The relative seismic quiescence before the mainshock and a magnitude of completeness $M_c^{min} \approx 2.0-2.5$ (Figures 3c-d) let us conclude that no significant foreshock occurred before the Sarez earthquake.

The aftershocks of the Sarez earthquake skirted around the co-seismic slip patch, with a concentration at the northern end of the rupture (Figure 4c; ∼60 km from the hypocenter) and sinistral transtensional focal mechanisms (Figure 4a). Aftershocks also concentrated ∼20 km south of the end of the co-seismically active fault patch (Figure 4c; -30 km), where the largest $M_W$5.3 aftershock $B*$ with a sinistral strike-slip mechanism similar to the Sarez mainshock occurred 102 days later; it spawned its own aftershock series (Fig-

ures 3c and 4d). An area of relative seismic quiescence between the southern end of the Sarez rupture and aftershock $B^*$ (between 10 and 30 km south of the Sarez hypocenter $A^*$, Figure 4d) may be attributed to the 1918 $M_W$6.6 earthquake that could have relaxed this segment (Figure 1b; Bondár et al., 2015).

The associated moment tensors exhibit both sinistral strike-slip and normal faulting mechanisms. Neither the co-, nor the post-seismic activity reactivated the ∼E-striking, Cenozoic thrusts and normal faults of this part of the Pamir (Figure 4a). The ∼NNE-strike of the normal-fault nodal planes are parallel to the many tensional surface-breaks mapped on ground along the northern segment (Figure 6 of Metzger et al., 2017) and the Quaternary-filled grabens, outlined on the 1:200,000 geological maps and traceable from topography (Figure 4a; Yushin et al., 1964). An important event of the earthquake sequence was the April 9, 2016 $M_W$4.1 dextral strike-slip event *c'* that occurred 124 days after the Sarez earthquake, ∼85 km north of the tip of its rupture plane, and 78 days before and ∼10 km east of the hypocenter of the Sary-Tash earthquake (Figures 3c, 4d, 5, 6).

### 5.2 Creep on the Sarez-Karakul Fault System

The accumulated InSAR line-of-sight (LOS) displacement between the Sarez and the Sary-Tash mainshocks shows a distinct change along the mapped SKFS (Figure 5a). While the data base of the southern frame is large enough to provide a good signal-to-noise ratio for detecting tectonic signals in the time-series, the resulting rates in the northern frame—based on 5 radar scenes—may be dominated by local atmospheric conditions (Figure S9).

The southern frame probably highlights sinistral motion and uplift east of the SKFS of ∼8 mm in the look direction between the first satellite pass on December 30, 2015 and the Sary-Tash earthquake (Figure 5a). The sinistral motion agrees with the co-seismic slip model of Metzger et al. (2017); the displacement amplitude is reasonable as well (∼1% of the co-seismic slip; Metzger et al., 2017), given that our observations do not capture the first three weeks of the post-seismic slip history.

In the northern frame, earthquake focal mechanisms indicate sinistral slip along the SKFS-segments north of Lake Karakul (Figure 4a; see also Schurr et al., 2014). Even though the view direction is nearly insensitive to lateral slip, we assume—due to the sig-

nificant across-strike displacement changes, the along-strike correlation of the signal, the seismic activity along the fault segments, and the location of events *c'* and *C** close to the northern tip of the SKFS—that the displacement signal is due to post-seismic creep on the SKFS; this allows to test whether creep may have contributed to the triggering of the Sary-Tash earthquake. The positive sign west of the SKFS (the ground moved towards the satellite) indicates that the signal is not due to a normal faulting component.

We modeled our displacement observations as aseismic slip on seven vertical fault patches between 0.5 and 10.5 km depth along two segments of the SKFS between the epicenters of the Sarez and the Sary-Tash earthquakes (Kokujbel segment in the south, Karakul segment in the north; Figures 4d and 5b). Our model indicates a maximum cumulative creep between 20 and 30 mm in the 202 days between the earthquakes on the Kokujbel segment (∼35–55 mm/yr, Figure S10), which occupies part of the slip patch of the Sarez earthquake. On the Karakul segment, we find a total maximum displacement of 40 mm (∼72 mm/yr) in the south to 25 mm (∼45 mm/yr, Figure S10) in the north. The segment links the co-seismically active part of the SKFS with the Kyzilart Transfer Zone, which connects the Muji Fault with the PFT (Figures 5a and 6a; Sippl et al., 2014)

### 5.3 Sary-Tash Earthquake

The Sary-Tash earthquake (*C** in Figures 3, 4, 5, 6; Table 1) occurred within the MPTS, westerly adjacent to the 2008 $M_W$6.6 Nura earthquake (Schurr et al., 2014; Sippl et al., 2014; Teshebaeva et al., 2014; Qiao et al., 2015). The region—geologically poorly-mapped in the high-altitude terrain of the Tajik-Kyrgyz-China border triangle—is characterized by a complex network of faults with both ∼N- and ∼S-dips, making the choice of the fault plane from the two nodal planes non-trivial. NEIC reports a comparatively low double-couple component for the mainshock moment tensor of 86%, hinting at the complexity of the rupture process.

The earthquake volume partially overlaps with the intense aftershock volume of the 2008 Nura earthquake (Sippl et al., 2014) and was seismically active throughout the different deployment periods of the various seismic networks covering the region; 13 small earthquakes ($M_L$1.6–3.7) were detected in the vicinity of the future Sary-Tash earthquake in the two months preceding the 2008 Nura earthquake during the TIPAGE deployment and 188 ($M_L$1.0–$M_W$4.4) in the 11 months before the Sary-Tash earthquake since the

8H network was active (Figures 3c, 6c and 6d). Foreshock activity was comparatively high compared to the Sarez and Muji mainshocks and peaked in 3 ∼1-month-long swarms in March, April and June 2016 (Figure 3c). Notably, the events that followed the April 9, 2016 foreshock *c'* concentrated around the future hypocenter $C^*$ in along-strike view (Figure 6c). The aftershocks of the Sary-Tash earthquake outlined an about vertical, ∼E-striking structure to ∼20 km depth east of the hypocenter (Figures 6b and 6e). Moment tensors display a variety of focal mechanisms, again testifying to a complex fault-zone (Figure 6a).

Fault-slip models of InSAR displacement maps slightly favor the steeply N-dipping nodal plane (FP1) over the gently ∼S-dipping one (FP2) for the Sary-Tash mainshock (He et al., 2018). If FP2 was the main fault plane, the aftershocks would crosscut it and be concentrated inside the volume of the largest slip (Figure 6b). This is contrary to what is observed for the Sarez (Section 5.1) and Muji (Section 5.5) earthquakes, and many other earthquakes worldwide, where aftershocks concentrate around the segments of highest slip (Das & Henry, 2003). We prefer the ∼N-dipping FP1 as the main fault plane, because with this choice the aftershocks are located in the hanging wall and up-dip of the largest co-seismic slip (Figure 6b), a pattern that has also been observed for the 2008 Nura earthquake (Sippl et al., 2014). The hypocenter is located at the western end of the geodetically-determined co-seismic slip patch (He et al., 2018), at 11.9 km depth, to the west and at 8.6 km hypocentral distance to the $M_W$4.4 foreshock *c'* (Figure 6e). The variable aftershock focal mechanisms tend to have dextral-transpressive mechanisms on ∼E-striking planes, except for two normal faulting events at the eastern end of the rupture (Figure 6a). The ∼E-striking nodal planes of the strike-slip solutions are interpreted to carry the dextral strike-slip deformation identified in the background seismicity of the TIPAGE deployment data and by geological fault-slip analysis within the MPTS and in the Kyzilart Transfer Zone; even the normal-fault earthquakes, indicating E–W extension, have neotectonic fault equivalents, and were interpreted as interaction of the SKFS with the MPTS (Sippl et al., 2014). The hypocenter depth and presumed N-dip of the Sary-Tash earthquake fault suggest that a basement fault in the footwall of the PFT got re-activated, as such faults are common in the Tian Shan immediately to the north (Figure 1b). In contrast, the 2008 Nura earthquake ruptured a ∼S-dipping plane; its hypocenter lay at 3.4 km depth and thus likely in the MPTS imbricate stack. That the Sary-Tash and Nura aftershock activities hardly overlap along strike, occupy different depth inter-

vals, and differently-dipping patches indicate that they activated different faults (Figures 6c and 6d). Another difference is that the shallow Nura earthquake re-activated several pre-existing NE- and NW-striking faults in the Tian Shan during its regionally-extensive aftershock sequence; the deeper Sary-Tash earthquake did not.

The Sarez earthquake caused a long-wavelength positive ΔCFS on the Sary-Tash earthquake fault with the highest values in the shallowest and westernmost part investigated. It loaded the rupture plane, foreshock *c'*, and hypocenter *C** only weakly (∼4 kPa; Table 1). Creep on the SKFS (Figure 5) additionally loaded the Sary-Tash earthquake fault, mainly in the upper westernmost part, but with a lobe of increased ΔCFS that reaches towards the hypocenter at ∼10 km depth (Figure 6g). East of the hypocenter, the foreshock *c'* loaded the rim of the rupture plane. Together they caused a ΔCFS concentration of $4^{+4}_{-3}$ kPa at the hypocenter (Table 1; Figure S14). Static stress change induced by the 2008 Nura earthquake loaded the fault in the order of ∼1 MPa (Figure S14). Despite this stress perturbation, the Sary-Tash earthquake did not rupture before 2016.

The area with the highest ΔCFS change west of the hypocenter did not rupture in an earthquake and did not produce many aftershocks (Figure 6e-f). It might be that the MPTS in this part—close to the intersection with the SKFS—has a different orientation than modeled. ΔCFS may therefore be smaller than modeled or even negative. It is also possible that the MPTS was not critically stressed, for example because it ruptured in an earlier unrecorded earthquake. Lastly, the fault properties of the adjacent segment may be such that it slips aseismically.

### 5.4 Muji Earthquake

153 days after the Sary-Tash earthquake, the $M_W$5.0 foreshock to the Muji earthquake *e'*, and its mainshock *E** occurred on the Muji Fault, ∼35 km southeast of the end of the rupture plane of the Sary-Tash earthquake. This configuration likely connects the MPTS in the area of the Sary-Tash earthquake with the Muji Fault along the Kyzilart Transfer Zone.

The rupture plane of the 2016 $M_W$6.6 Muji earthquake (*E** in Figures 3, 6, and 7; Table 1) broke nearly simultaneously in two main slip patches; a third slip patch, modeled below ∼20 km depth, is unresolved (Bie et al., 2018). The area of the eastern slip patch was seismically active during the TIPAGE (2008–2010) and the current deploy-

ment (2015–2017; Figure 7b). The $M_W$5.0 Muji foreshock *e'* occurred only 12 minutes before the mainshock, at the western end of the rupture plane and ∼460 m hypocentral distance (Figures 7a and 7b). We identified a series of four more foreshocks between *e'* and *E** in the seismogram of the closest station EP10 but could not locate them. The mainshock hypocenter was at 13.7 km depth. Aftershocks concentrated around and below the highest slip zone at the WNW end of the rupture plane, tightly constrained to the rim of the main slip patch; they continued ∼10 km beyond its ESE' end of the eastern slip patch (Figure 7c). The western continuation of the Muji fault remained seismically relatively quiet.

Fore- and aftershock moment tensors exhibit dextral focal mechanisms similar to the mainshock. Notably, the two western focal mechanisms have a small reverse faulting component, while the two eastern ones have a small normal faulting component, a fault kinematic that was also observed in the morphology of the surface breaks (T. Li et al., 2019). This is compatible with the transition from the nearly purely extensional faulting along the Kongur Shan Normal Fault System to the dextral-transpressional Kyzilart Transfer Zone and MPTS.

The preferred ΔCFS model for the Muji earthquake (Figure 7d) suggests that the Sarez and Sary-Tash earthquakes unloaded the fault plane with a negative ΔCFS of $-19^{+7}_{-6}$ kPa (Figures S12 and S15; Table 1). For the Sarez earthquake, the effect is mostly due to clamping of the Muji fault through normal stress and a slight loading opposite to the slip sense, i.e., a relaxation. The Sary-Tash earthquake imposed sinistral strain on the Muji fault, as it pulled the northern wall more towards the northwest relative to the southern wall; this is opposite to the dextral slip of the earthquake. The 2008 Nura earthquakes also imposed sinistral slip on the Muji fault, unloading it similarly to the Sary-Tash earthquake.

The foreshock *e'* stressed the hypocenter with ΔCFS ≈ 60 kPa. However, the remainder of the fault plane remained in the unloaded and clamped state described above and—as the foreshock has a focal mechanism and location almost identical to the mainshock—our model can neither explain triggering of *e'* through CFS changes. We conclude that static stress changes counteracted the pending Muji rupture and that rupture must have occurred due to another trigger.

The occurrence of aftershocks east of the Muji mainshock rupture plane but not west of it may suggest that the western continuation of the Muji Fault was not critically stressed; either because it has been relaxed by the sinistral far-field strain of the 2008 Nura and 2016 Sary-Tash earthquakes, as indicated by our stress model (Figure 7d), or because it already slipped in an unrecorded earthquake or an undetected slip transient on the Kyzilart Transfer Zone. A candidate for an earthquake that filled this seismic gap may be the 1974 Markansu earthquake (Figure 1b). It has been located (Fan et al., 1994) and re-located (Sippl et al., 2014) within the MPTS. Full-waveform inversion suggests a complex thrust mechanism similar to the 2008 Nura earthquake (Langston & Dermengian, 1981), but some authors advocate for a dextral strike-slip mechanism similar to the Muji earthquake (Burtman & Molnar, 1993), which would be consistent with the expected slip sense on the quiet segment of the Muji fault. Lastly, the properties of the fault segment might be such that it creeps aseismically.

### 5.5 Northwest Pamir Earthquake Swarm

An earthquake swarm of 80 events occurred on the western side of Pamir's Academy of Sciences Range, hosting Pamir's highest peaks ($D$ in Figures 3 and 8; Table 1). It was active throughout the deployment of the Sarez aftershock network (Figure 3c), with an activity peak, including the largest $M_W$4.6 event $D^*$, in August 2016. Focal mechanisms indicate normal faulting on ∼N(NW)-striking planes. Well-located hypocenters and moment tensor centroids show that most seismicity clustered at shallow depth (≤6 km; Figure 8). Such normal-faulting solutions are—together with strike-slip solutions—typical for the western Pamir, the part of the Pamir Plateau that shows westward-increasing collapse of crust into the Tajik Depression (Kufner et al., 2018; Schurr et al., 2014).

### 5.6 Yarkant Earthquake

On January 20, 2017 an $M_W$5.0 earthquake occurred 53 km southwest of Yarkant, Xinjiang ($F^*$ in Figures 3 and 8; Table 1). Three events were detected in its volume $F$ before the earthquake—one of them only 55 minutes before the mainshock—and a total of 41 aftershocks. The moment tensor indicates thrusting on either a shallowly- or a steeply-dipping fault plane. Seismicity aligns along a ∼N-striking structure (Figure 8), paralleling the topographic slope and the strike of the shallowly-dipping nodal plane. We

interpret these earthquakes to record top-to-NE thrusting along ∼SW-dipping faults, compatible with the growth of the eastern Pamir into the Tarim Basin (Figures 1 and 8).

### 5.7 Khorog Earthquake

On March 22, 2017, a $M_W$4.9 earthquake occurred ∼51 km ENE of Khorog, Tajikistan ($G^*$ in Figures 3 and 8; Table 1). Our ΔCFS model suggests a stressing of ∼12 kPa by the Sarez earthquake. The volume $G$ of the earthquake was active throughout the deployment of the 9H network with 24 seismic events detected before the mainshock. Whether the structure was activated by the Sarez earthquake—whose hypocenter is located ∼90 km NE of the earthquake—is unclear, because of the limited sensitivity of the network before the 9H network deployment. Two ∼NE-trending streaks of seismic activity can be identified in map view; the focal mechanism indicates sinistral strike-slip on a ∼NE-striking fault. The depth of the earthquake is not well constrained due to the limited network coverage (Figure 8). The earthquake cluster lies along a fault zone classified as likely active by Stübner et al. (2013) and Schurr et al. (2014) due to linear topographic expressions; the fault zone coincides with the southeastern part of the Pathus-Nemos Fault of Strom (2014); it overprints the Miocene dextral-normal Gund shear/fault zone at an acute angle (Figure 1b; Worthington et al., 2020). As a mappable continuation of the neotectonic fault network at the southern continuation of the SKFS (Figure 1b), we interpret the Khorog earthquake cluster as part of the distributed faults that connect the SKFS with the sinistral fault zones of the Hindu Kush (e.g., the Chaman, Panjshir, Central Badakhshan Fault Zones; Figure 1b), outlining a continuous fault zone along the western edge of the Indian indenter at mantle depth (Section 2; Metzger et al., 2017).

Elliott et al. (2020) proposed this fault zone as the source of the 1911 Sarez earthquake. The relative seismic quiescence between the Sarez aftershock $B^*$ and the Khorog earthquake $G^*$ (Figure 8 and S16a) may suggest that the ∼ 30 km long fault segment in between was not critically stressed, perhaps due to the 1911 earthquake.

### 5.8 Karamyk Earthquake

An $M_W$6.0 earthquake happened on May 3, 2017 near the Kyrgyz-Tajik border, ∼25 km west of the settlement of Karamyk, Kyrgyzstan ($H^*$ in Figures 3 and 8; Table 1). The event was outside of the network, but due to the relatively large magnitude some

aftershock seismicity could be located and the moment tensors of the mainshock and one aftershock be determined. The seismicity outlined a ∼NE-trending cluster, with a dextral strike-slip- and a reverse-faulting focal mechanism for the mainshock and an aftershock, respectively (Figure 8). The cluster lies along a Cenozoic fault zone in the Tian Shan, outlined by partly overthrusted Jurassic-Paleogene basin strata; geological fault-slip analysis along the eastern strands of these fault zone reveals top-to-NW thrusting with a dextral strike-slip component (stations TS19 to TS22 in Figure S7 in Kufner et al., 2018).

### 5.9 Taxkorgan Earthquake

The last moderate earthquake detected during our recording period was the $M_W$5.4 Taxkorgan earthquake on May 10, 2017, ∼23 km south of Taxkorgan, Xinjiang ($I^*$ in Figures 3 and 8; Table 1). Aftershock seismicity and the focal mechanism indicate that it reactivated a steeply ∼ENE-dipping segment of the Taxkorgan Normal Fault (Robinson et al., 2007). 14 foreshocks preceded the earthquake, half of them in the two months after the Muji earthquake (Figures 3 and 8). The Taxkorgan Normal Fault can be interpreted as part of the Kongur Shan–Taxkorgan Normal Fault System, with a southward decreasing amount of extension (Figure 1).

## 6 Regional Stress Field

The tectonic interpretation resolved the nodal plane ambiguity of most moment tensors. We inverted the resultant slip vector orientations for the regional deviatoric unit stress tensor $\hat{S}$ by minimizing the misorientation between the slip vector and the predicted largest shear stress on the fault plane, using the *slick* toolbox (Michael, 1984, 1987). In north–east–down-convention:

$$\hat{S} = \begin{pmatrix} -0.798 & 0.596 & -0.004 \\ 0.596 & 0.867 & 0.177 \\ -0.004 & 0.177 & -0.069 \end{pmatrix} \tag{9}$$

This indicates near-horizontal, N18°W-oriented compression $\sigma_1$, N72°E-oriented extension $\sigma_3$, and a 81° SW-plunging $\sigma_2$ (Figure 8). The relative magnitudes of $\sigma_1$, $\sigma_2$, and $\sigma_3$ are -0.99, -0.09, and 1.08. The stress field is dominantly strike-slip with a reverse faulting component. $\sigma_1$ is about parallel to the GNSS vectors in the Pamir interior and $\sigma_1$ at mantle depth (Bloch et al., 2021). $\sigma_2$ has a compressional component, represented by

the shape factor $\frac{\sigma_2-\sigma_1}{\sigma_3-\sigma_1} = 0.44$, or the compensated linear vector dipole component of the stress tensor of 17%. We interpret the vertical compression component to reflect the bulk thinning of the crust of the Pamir Plateau due to its westward (along the $\sigma_3$-orientation) collapse into the Tajik Depression.

# 7 Discussion

## 7.1 Seismotectonics

Tectonically, the earthquake sequence recorded between August 2015 and July 2017 outlines the first-order deformation field of the Pamir and southernmost Tian Shan. The northward displacement of the eastern Pamir Plateau, tied to the Tarim-Basin lithosphere, is absorbed to a large extent along the Pamir front, the MPTS. Basement-rooted faults of the Paleozoic Tian Shan orogen, that have been re-activated since ∼12 Ma (e.g. Käßner et al., 2016; Abdulhameed et al., 2020), most recently yielded during the the Sary-Tash ($C$) and Karamyk ($H$) earthquakes on both ends of the Alai Valley, where the MPTS interacts with the Tian Shan. This requires the activation of a basal detachment deeper than that of the MPTS in Jurassic evaporites, that governs the fold-thrust belt of the Tajik Depression (e.g. Bekker, 1996; Gagała et al., 2020). About E–W extension in the eastern Pamir along the Kongur Shan-Taxkorgan Normal Fault System ($I$), with northward increasing amounts (Robinson et al., 2007), is transferred into dextral strike-slip along the Muji Fault, and—under increasingly transpressional deformation—via the western Muji Fault and the Kyzilart Transfer Zone into and across the MPTS to the PFT; the latter is characterized by range-front segmentation in thrusts and dextral strike-slip faults (e.g. Arrowsmith & Strecker, 1999; Sippl et al., 2014).

The Pamir Plateau is dissected by the SKFS into the relative aseismic eastern Pamir block and the western Pamir with higher seismic activity (Schurr et al., 2014). Although we concur with the interpretation that the SKFS is part of the broad and distributed zone of sinistral strike-slip faulting along the western margin of the Indian mantle lithosphere indenter (Metzger et al., 2017), several aspects of this fault zone are particular: (1) The two largest historical crustal earthquakes of the Pamir interior—the 1911 and 2015 Sarez earthquakes—occurred at the southern end of the SKFS, approximately above the northeastern tip of the indenter (Figure 1b); (2) the SKFS is morphologically well-expressed along the Sarez, Kokujbel, and Karakul segments, but loses expression enter-

ing the MPTS and the southwestern Pamir; (3) neotectonically, the northern Kokujbel and Karakul segments show the clearest evidence of ∼E-W extension, suggesting a northward increasing extensional component (from the Sarez to the Karakul segments), akin to that of the Kongur-Shan-Taxkorgan Normal Fault System. We speculate that the SKFS nucleated above the tip of the indenter and has been growing towards the NE and SW. The northward-increasing transtensional component in the Sarez aftershocks, the rift appearance of the Karakul segment, the anticlockwise change in strike of the northernmost SKFS segments, and the (little-studied) merger of these strands with the MPTS (Figures 1b and 4) suggest increasingly stronger westward motion of material from the eastern Pamir in the east to the Tajik Depression to the west, and from the Hindu Kush and Karakorum in the south to the front of the Pamir in the north; this is traced by the GNSS velocity vectors (Figure 1b; Metzger et al., 2020) and the anticlockwise rotations recorded in the northern Tajik Depression by paleomagnetic data (Pozzi & Feinberg, 1991; Thomas et al., 1994). The SKFS at and south of Lake Sarez and the dextral Aksu-Murghab Fault Zone and its western prolongation, the Sarez-Murghab Thrust System, may outline—on first-order—the triangular shape of the tip of the mantle indenter by distributed deformation in the crust (Figures 1 and 8).

While the eastern Pamir is growing outward into the Tarim basin by thrusting ($F$), the entire western Pamir has a significant component of ∼E-W extension, reflecting its collapse into the Tajik Depression. The westward increasing extensional component is accommodated by an increase in the dextral strike-slip component along the western MPTS e.g., the Vakhsh Thrust System; Figure 1b; Metzger et al. (2020), and the involvement of the southern Tian Shan in the Pamir deformation field by thrusting and dextral strike-slip faulting ($H$; for the similar neotectonic evolution see Käßner et al., 2016).

## 7.2 Earthquake Triggering

### *7.2.1 Stress Triggering*

We argued at the outset that the probability of the three largest earthquakes occurring by chance in such close vicinity in space and time is very low and tested if static CFS changes from the consecutive earthquake ruptures are able to explain rupture triggering of the neighboring faults. ΔCFS has a strong effect in the near field but diminishes rapidly at distances greater than about one rupture length. It is positive between

10s and 100s kPa for the aftershocks that occurred at distances of 5–50 km in the extension of the Sarez rupture and may be a viable trigger for the moderate earthquakes in the southern continuation of the SKFS (e.g., events *B**, *G**, Table 1) and the aftershocks to the north spanning Lake Karakul (e.g., events *2*, *4*, *28*; Table 1; Figure 8). Earthquakes located at large distances from any large earthquakes (>100 km; *F**, *H**, *I**) received no more than a miniscule ΔCFS and occurred likely independent of the large mainshocks.

For the Sary-Tash earthquake—that motivated this study—and its foreshock *c'*, ΔCFS may be as low as 4 kPa, if possible creep along the SKFS is ignored. Even with creep and favorable (low-$\beta$) fault parameters, ΔCFS at the Sary-Tash hypocenter does not exceed 10 kPa (Figure S15; see also Fialko et al., 2021). These values may be just above the tidal shear stresses that the dip-slip fault experiences over the course of a day (∼5 kPa; Tanaka et al., 2002). An additional ΔCFS contribution may be caused by viscous relaxation of the lower crust in the months following the Sarez earthquake, which would constitute an additional, deeper source with the same sense of motion and therefore a comparable effect as the earthquake itself. The time constant inherent to viscous processes might account for the time lag of 7 months between events *A** and *C** to over 15 months between event *A** and *G** (Table 1). But the modeling of the post-seismic slip of the Sarez earthquake suggests that no visco-elastic relaxation took place (Fialko et al., 2021). Slip–rate-dependent friction may account for the observed time lag and imply undetected, accelerating pre-slip on the fault (Dieterich, 1992). But the foreshock rate on the fault is not accelerating (Figure 3c) and there is no other data that would support this hypothesis.

In case of the Muji foreshock *e'*, negative ΔCFS values indicate stabilization at the hypocenter and suggest that it ruptured *despite of*—not due to—the static stress changes imposed by the previous earthquakes. We cannot exclude that the complexity of the Sary-Tash earthquake, indicated by the diverse aftershock mechanisms and the high compensated linear vector dipole component of the moment tensor, may have caused a more complex deformation pattern below the MPTS, but we consider it unlikely that it reversed the modeled stress relaxation. Undetected triggered dextral creep on the Kyzilart Transfer Zone—that connects the PFT with the Muji Fault—may have imposed a positive ΔCFS that loaded the foreshock hypocenter. That foreshock activity is at most weakly dependent on previous mainshock occurrence (Figure 3) corroborates the inference that the static stress changes contributed only little to the total stress budget of the faults. The

699 consistency between the earthquake moment tensor and the regional stress tensor (Fig-
700 ure 8) implies that the earthquake responded to the long-term tectonic loading.

701 Beyond the near-field, where ΔCFS dominates, dynamic stress changes probably
702 play an important role to generate aftershocks (Felzer & Brodsky, 2006) or even trigger
703 remote earthquakes (Gomberg & Johnson, 2005). But dynamic stresses act almost im-
704 mediately and do not provide an explanation for the multi-month delays between the events.

705 #### *7.2.2 Fluid Triggering*

706 That the observed seismicity, i.e., the three major sequences but also the moder-
707 ate ones, appears to occur at a with time increasing distances from the Sarez earthquake
708 rupture that mimic a diffusion law (Figure 3e, Equation 8), may point at an important
709 contribution of fluid migration to the earthquake triggering. Pore pressure counteracts
710 normal stress and has a decisive effect on the frictional stability of faults. Faults are hy-
711 drological systems that store fluids if they are sealed and guide them if they are perme-
712 able. In sealed fault systems, fluids may be pressurized. An earthquake may breach seals
713 and mobilize the fluids (Sibson, 1992). Brittle damage generated by the mainshock and
714 aftershocks can increase permeability of fault zones by orders of magnitude (Kitagawa
715 et al., 2002; Miller & Nur, 2000), particularly in the damage zones surrounding the fault
716 cores, making them perfect transportation pathways for fluids (Miller, 2020). There is
717 strong geophysical indication for fluids in Pamir's upper crust that contains the fault sys-
718 tems discussed here: a magneto-telluric profile—traversing the Pamir near the Sary-Tash
719 earthquake—showed high-conductivity regions across the MPTS that were interpreted
720 as due to aqueous fluids within the damage zones (Sass et al., 2014). This is corrobo-
721 rated by significantly increased P- to S-wave velocity ratios in the upper ∼10 km of the
722 crust along the MPTS detected by tomography (Sippl, Schurr, Tympel, et al., 2013). A
723 contribution of poro-elastic rebound is consistent with the post-seismic deformation pat-
724 tern of the Sarez earthquake (Fialko et al., 2021). The fault zones that ruptured dur-
725 ing the three major earthquakes are almost adjoining and likely interconnected. We hy-
726 pothesize that fluids captured in the fault zone of the Sarez earthquake were co-seismically
727 freed and pressured along the SKFS where permeability may have been increased by brit-
728 tle fracturing and transient stress changes (Manga et al., 2012; Fitzenz & Miller, 2001),
729 generating aftershocks, reaching the MPTS and triggering the Sary-Tash earthquake. This
730 may have initiated another fluid pressure wave sweeping through the fracture mesh con-

necting the MPTS and the Muji fault zone, eventually triggering the third event. Fluid triggering of the Muji earthquake may also account for the near-simultanous rupture of both slip patches (Bie et al., 2018). The progression of a fluid front with time may be described by the square-root envelope-function of Equation 8. Seismic event clouds that expand according to such a relationship are regularly observed in controlled fluid injection scenarios, such as hydrologically fracturing geothermal reservoirs (Shapiro et al., 2003). Our estimates for the hydraulic diffusivity ($D \approx 12$–$40\,\mathrm{m^2/s}$; Figure 3e) are stable with respect to the choice in origin (Figure S16). Setting a new origin at the eastern end of the Sary-Tash earthquake for the later sweep to the Muji earthquake results in the same values. $D \approx 12$–$40\,\mathrm{m^2/s}$ is well within the range suggested by Shapiro et al. (2003) of $10^{-2}$ to $10^{-1}\,\mathrm{m^2/s}$ for crystalline rocks to $10^{2}\,\mathrm{m^2/s}$ for a recently ruptured subduction megathrust fault.

Whether the more isolated sequences ($H$ and $I$, Figures 3a and 8) were also reached by a fluid front is unclear. The swarm-like normal faulting sequence $D$, overlapping with the Sarez earthquake sequence, may have been initiated by dynamic perturbation of the hydraulic system through transient stresses from strong shaking, as has frequently been observed (Manga et al., 2012). In the present case, only the larger earthquakes appear to have occurred when a fluid front has passed. The weak and relatively abundant foreshock seismicity occurred independently and earlier. The slightly increased foreshock rate on all but the Sarez rupture planes compared to the observation period of the TIPAGE experiment (2008–2010) suggests that the initial mainshock perturbed the local fault properties immediately, even though transferred stresses were low or negative and the suggested fluid front has not yet arrived.

## 8 Conclusion

We analyzed the seismic record of the earthquake sequence that struck the Pamir highlands in 2015–2017 in detail. Our observation started ∼4 months before the initial $M_W$7.2 Sarez earthquake, for which no significant precursory seismic activity could be detected. The subsequent $M_W$6.4 Sary-Tash and $M_W$6.6 Muji earthquakes on adjacent faults, but more than 80 km away showed foreshock activity, as did other $M_W$4.4–5.7 earthquakes in the region. Aftershock seismicity traced the activated fault zones and testified to the Pamir Plateau dissecting nature of the Sarez Karakul Fault System, interaction of the Main Pamir Thrust System with the northerly adjacent Tian Shan, and

growth of the Pamir over the Tarim Basin in the east. Static stress transfer from the mainshocks, postseismic deformation and moderate foreshocks contributed at most subordinately to the stress budget of the activated fault segments. More likely, fluids migrating through the damaged fault zones and triggered the subsequent earthquakes. An improved detection and quantification of such fluid processes is required to gain a better understanding of the mechanisms that trigger seismicity during periods of seismic unrest.

**Acknowledgments**

We thank the drivers and field participants from the Institute of Tibetan Plateau Research, especially Hongbing Liu, who helped to organize the station deployment; Christian Sippl, Sebastian Hainzl, and Rongjiang Wang for sharing code and discussion; Serge A. Shapiro for discussion; and Ayleen Gaete for assisting the data processing. Funded by the CaTeNA project of the German Federal Ministry of Science and Education (support codes 03G0878A and 03G0878B) and German Research Council project RA 442/41. Open Access facilitated through project DEAL. Seismic data were handled using *obspy* (Krischer et al., 2015) and *pyrocko* (Heimann et al., 2017). Figures were created with the help of the *Generic Mapping Tools* (Wessel et al., 2013), *maplotlib* (Hunter, 2007) and *Scientific Color Maps* (Crameri et al., 2020). Part of the instruments were provided by GIPP of GFZ Potsdam. Seismic data are archived in the GEOFON data center. The seismic event and moment tensor catalogs are available through GFZ data services (`https://dataservices.gfz-potsdam.de`; Bloch et al., 2022). LiCSAR (Looking into the Continents from Space) contains modified Copernicus Sentinel data analysed by the Centre for the Observation and Modelling of Earthquakes, Volcanoes and Tectonics (COMET; `https://comet.nerc.ac.uk/comet-lics-portal`) LiCSAR uses JASMIN, the UK's collaborative data analysis environment (`https://jasmin.ac.uk`).

## References

Abdulhameed, S., Ratschbacher, L., Jonckheere, R., Gagała, Ł., Enkelmann, E., Käßner, A., ... others (2020). Tajik basin and southwestern Tian Shan, northwestern India-Asia collision zone: 2. Timing of basin inversion, Tian Shan mountain building, and relation to Pamir-plateau advance and deep India-Asia indentation. *Tectonics*, *39*(5), e2019TC005873.

Aldersons, F. (2004). Toward three-dimensional crustal structure of the Dead Sea region from local earthquake tomography. *PhD thesis*.

Arrowsmith, J. R., & Strecker, M. (1999). Seismotectonic range-front segmentation and mountain-belt growth in the Pamir-Alai region, Kyrgyzstan (India-Eurasia collision zone). *Geological Society of America Bulletin*, *111*(11), 1665–1683.

Bekker, Y. A. (1996). Tectonics of the Afghan-Tajik depression. *Geotectonics*, *30*(1), 64–70.

Bie, L., Hicks, S., Garth, T., Gonzalez, P., & Rietbrock, A. (2018). 'Two go together': Near-simultaneous moment release of two asperities during the 2016 Mw 6.6 Muji, China earthquake. *Earth and Planetary Science Letters*, *491*, 34–42. doi: 10.1016/j.epsl.2018.03.033

Bloch, W., Schurr, B., Yuan, X., Ratschbacher, L., Reuter, S., Kufner, S.-K., ... Zhao, J. (2021). Structure and stress field of the lithosphere between Pamir and Tarim. *Geophysical Research Letters*, *48*(22). doi: 10.1029/2021gl095413

Bloch, W., Schurr, B., Yuan, X., Xu, Q., Zhao, J., Murodkulov, S., & Oimuhammadzoda, I. (2022). Earthquake and moment tensor catalogs of the 2015–2017 Pamir earthquake sequence. *GFZ Data Services*. doi: 10.5880/fidgeo.2022.007

Bondár, I., Engdahl, E. R., Villaseñor, A., Harris, J., & Storchak, D. (2015). ISC-GEM: Global instrumental earthquake catalogue (1900–2009), II. location and seismicity patterns. *Physics of the Earth and Planetary Interiors*, *239*, 2–13. doi: 10.1016/j.pepi.2014.06.002

Bormann, P., & Dewey, J. W. (2012). The new IASPEI standards for determining magnitudes from digital data and their relation to classical magnitudes. In *New Manual of Seismological Observatory Practice 2 (NMSOP-2)* (pp. 1–44). Deutsches GeoForschungsZentrum GFZ. doi: https://doi.org/10.2312/GFZ.NMSOP-2_IS_3.3

Bouchon, M. (1981). A simple method to calculate Green's functions for elastic layered media. *Bulletin of the Seismological Society of America*, *71*(4), 959–971.

Burtman, V. S., & Molnar, P. H. (1993). *Geological and geophysical evidence for deep subduction of continental crust beneath the Pamir* (Vol. 281). Geological Society of America.

Chen, K., Avouac, J.-P., Aati, S., Milliner, C., Zheng, F., & Shi, C. (2020). Cascading and pulse-like ruptures during the 2019 Ridgecrest earthquakes in the

Eastern California Shear Zone. *Nature communications*, *11*(1), 1–8.

Chevalier, M.-L., Pan, J., Li, H., Liu, D., & Wang, M. (2015). Quantification of both normal and right-lateral late Quaternary activity along the Kongur Shan extensional system, Chinese Pamir. *Terra Nova*, *27*(5), 379–391.

Cocco, M., & Rice, J. R. (2002). Pore pressure and poroelasticity effects in coulomb stress analysis of earthquake interactions. *Journal of Geophysical Research: Solid Earth*, *107*(B2), ESE 2-1-ESE 2-17. Retrieved from `https://agupubs.onlinelibrary.wiley.com/doi/abs/10.1029/2000JB000138` doi: https://doi.org/10.1029/2000JB000138

Comino, J. Á. L., Heimann, S., Cesca, S., Milkereit, C., Dahm, T., & Zang, A. (2017). Automated full waveform detection and location algorithm of acoustic emissions from hydraulic fracturing experiment. *Procedia engineering*, *191*, 697–702.

Cowgill, E. (2009). Cenozoic right-slip faulting along the eastern margin of the Pamir salient, northwestern China. *Geological Society of America Bulletin*, *122*(1-2), 145–161. doi: 10.1130/b26520.1

Crameri, F., Shephard, G. E., & Heron, P. J. (2020). The misuse of colour in science communication. *Nature communications*, *11*(1), 1–10.

Das, S., & Henry, C. (2003). Spatial relation between main earthquake slip and its aftershock distribution. *Reviews of Geophysics*, *41*(3). Retrieved from `https://agupubs.onlinelibrary.wiley.com/doi/abs/10.1029/2002RG000119` doi: https://doi.org/10.1029/2002RG000119

Diehl, T., Deichmann, N., Kissling, E., & Husen, S. (2009). Automatic S-wave picker for local earthquake tomography. *Bulletin of the Seismological Society of America*, *99*(3), 1906–1920.

Dieterich, J. H. (1992). Earthquake nucleation on faults with rate-and state-dependent strength. *Tectonophysics*, *211*(1-4), 115–134. doi: 10.1016/0040-1951(92)90055-b

Di Giacomo, D., Engdahl, E. R., & Storchak, D. A. (2018). The ISC-GEM earthquake catalogue (1904–2014): status after the extension project. *Earth System Science Data*, *10*(4), 1877–1899.

Elliott, A., Elliott, J., Hollingsworth, J., Kulikova, G., Parsons, B., & Walker, R. (2020). Satellite imaging of the 2015 M 7.2 earthquake in the Central Pamir,

Tajikistan, elucidates a sequence of shallow strike-slip ruptures of the Sarez-Karakul fault. *Geophysical Journal International*, *221*(3), 1696–1718.

Ellsworth, W. L., & Bulut, F. (2018). Nucleation of the 1999 Izmit earthquake by a triggered cascade of foreshocks. *Nature Geoscience*, *11*(7), 531–535.

Fan, G., Ni, J. F., & Wallace, T. C. (1994). Active tectonics of the Pamirs and Karakorum. *Journal of Geophysical Research: Solid Earth*, *99*(B4), 7131–7160. doi: 10.1029/93jb02970

Felzer, K. R., & Brodsky, E. E. (2006). Decay of aftershock density with distance indicates triggering by dynamic stress. *Nature*, *441*(7094), 735–738.

Fialko, Y., Jin, Z., Zubovich, A., & Schöne, T. (2021). Lithospheric deformation due to the 2015 M7.2 Sarez (Pamir) earthquake constrained by 5 years of space geodetic observations. *Earth and Space Science Open Archive*, 49. Retrieved from `https://doi.org/10.1002/essoar.10508106.1` doi: 10.1002/essoar.10508106.1

Fitzenz, D. D., & Miller, S. A. (2001). A forward model for earthquake generation on interacting faults including tectonics, fluids, and stress transfer. *Journal of Geophysical Research: Solid Earth*, *106*(B11), 26689–26706.

Freed, A. M., & Lin, J. (2001). Delayed triggering of the 1999 Hector Mine earthquake by viscoelastic stress transfer. *Nature*, *411*(6834), 180–183.

Gagała, Ł., Ratschbacher, L., Ringenbach, J.-C., Kufner, S.-K., Schurr, B., Dedow, R., ... Oimahmadov, I. (2020). Tajik Basin and Southwestern Tian Shan, Northwestern India-Asia Collision Zone: 1. Structure, Kinematics, and Salt Tectonics in the Tajik Fold-and-Thrust Belt of the Western Foreland of the Pamir. *Tectonics*, *39*(5), e2019TC005871.

Gomberg, J., & Johnson, P. (2005). Dynamic triggering of earthquakes. *Nature*, *437*(7060), 830–830.

Harris, R. A. (1998). Introduction to special section: Stress triggers, stress shadows, and implications for seismic hazard. *Journal of Geophysical Research: Solid Earth*, *103*(B10), 24347–24358.

He, P., Hetland, E. A., Niemi, N. A., Wang, Q., Wen, Y., & Ding, K. (2018). The 2016 Mw 6.5 Nura earthquake in the Trans Alai range, northern Pamir: possible rupture on a back-thrust fault constrained by Sentinel-1A radar interferometry. *Tectonophysics*, *749*, 62–71.

Heimann, S., Kriegerowski, M., Isken, M., Cesca, S., Daout, S., Grigoli, F., ... others (2017). Pyrocko - An open-source seismology toolbox and library. *GFZ Data Services*. doi: https://doi.org/10.5880/GFZ.2.1.2017.001

Hooper, A. (2008). A multi-temporal insar method incorporating both persistent scatterer and small baseline approaches. *Geophysical Research Letters*, *35*(16). Retrieved from `https://agupubs.onlinelibrary.wiley.com/doi/abs/10.1029/2008GL034654` doi: https://doi.org/10.1029/2008GL034654

Hunter, J. D. (2007). Matplotlib: A 2D graphics environment. *Computing in Science & Engineering*, *9*(3), 90–95. doi: 10.1109/MCSE.2007.55

ISC. (2021). *ISC-GEM Earthquake Catalogue* (Tech. Rep.). International Seismological Centre. doi: https://doi.org/10.31905/d808b825

Ischuk, A., Bendick, R., Rybin, A., Molnar, P., Khan, S. F., Kuzikov, S., ... others (2013). Kinematics of the Pamir and Hindu Kush regions from GPS geodesy. *Journal of Geophysical Research: Solid Earth*, *118*(5), 2408–2416.

Isken, M., Sudhaus, H., Heimann, S., Steinberg, A., Daout, S., & Vasyura-Bathke, H. (2017). Kite-software for rapid earthquake source optimisation from InSAR surface displacement. *GFZ Data Services*. doi: 10.5880/GFZ.2.1.2017.002

Jade, S., Bhatt, B., Yang, Z., Bendick, R., Gaur, V., Molnar, P., ... Kumar, D. (2004). GPS measurements from the Ladakh Himalaya, India: Preliminary tests of plate-like or continuous deformation in Tibet. *Geological Society of America Bulletin*, *116*(11-12), 1385–1391.

Käßner, A., Ratschbacher, L., Jonckheere, R., Enkelmann, E., Khan, J., Sonntag, B.-L., ... Oimahmadov, I. (2016). Cenozoic intracontinental deformation and exhumation at the northwestern tip of the India-Asia collision—southwestern Tian Shan, Tajikistan, and Kyrgyzstan. *Tectonics*, *35*(9), 2171–2194.

Kissling, E., Ellsworth, W., Eberhart-Phillips, D., & Kradolfer, U. (1994). Initial reference models in local earthquake tomography. *Journal of Geophysical Research: Solid Earth*, *99*(B10), 19635–19646.

Kitagawa, Y., Fujimori, K., & Koizumi, N. (2002). Temporal change in permeability of the rock estimated from repeated water injection experiments near the Nojima fault in Awaji Island, Japan. *Geophysical research letters*, *29*(10), 121–1.

Kreemer, C., Blewitt, G., & Klein, E. C. (2014). A geodetic plate motion and global

strain rate model. *Geochemistry, Geophysics, Geosystems*, *15*(10), 3849–3889.

Krischer, L., Megies, T., Barsch, R., Beyreuther, M., Lecocq, T., Caudron, C., & Wassermann, J. (2015). ObsPy: A bridge for seismology into the scientific Python ecosystem. *Computational Science & Discovery*, *8*(1), 014003.

Kufner, S.-K., Kakar, N., Bezada, M., Bloch, W., Metzger, S., Yuan, X., ... others (2021). The Hindu Kush slab break-off as revealed by deep structure and crustal deformation. *Nature communications*, *12*(1), 1–11.

Kufner, S.-K., Schurr, B., Haberland, C., Zhang, Y., Saul, J., Ischuk, A., & Oimahmadov, I. (2017). Zooming into the Hindu Kush slab break-off: A rare glimpse on the terminal stage of subduction. *Earth and Planetary Science Letters*, *461*, 127–140.

Kufner, S.-K., Schurr, B., Ratschbacher, L., Murodkulov, S., Abdulhameed, S., Ischuk, A., ... Kakar, N. (2018). Seismotectonics of the Tajik basin and surrounding mountain ranges. *Tectonics*, *37*(8), 2404–2424.

Kufner, S.-K., Schurr, B., Sippl, C., Yuan, X., Ratschbacher, L., Ischuk, A., ... others (2016). Deep India meets deep Asia: Lithospheric indentation, delamination and break-off under Pamir and Hindu Kush (Central Asia). *Earth and Planetary Science Letters*, *435*, 171–184.

Kulikova, G., Schurr, B., Krüger, F., Brzoska, E., & Heimann, S. (2016). Source parameters of the Sarez-Pamir earthquake of 1911 February 18. *Geophysical Journal International*, *205*(2), 1086–1098.

Langston, C. A., & Dermengian, J. M. (1981). Comment on 'seismotectonic aspects of the Markansu Valley, Tadjikstan, earthquake of august 11, 1974' by James Jackson, Peter Molnar, Howard Patton, and Thomas Fitch. *Journal of Geophysical Research: Solid Earth*, *86*(B2), 1091–1093. doi: 10.1029/jb086ib02p01091

Lazecký, M., Spaans, K., González, P. J., Maghsoudi, Y., Morishita, Y., Albino, F., ... Wright, T. J. (2020). Licsar: An automatic insar tool for measuring and monitoring tectonic and volcanic activity. *Remote Sensing*, *12*(15). Retrieved from `https://www.mdpi.com/2072-4292/12/15/2430` doi: 10.3390/rs12152430

Lee, W. H. K., & Lahr, J. C. (1972). *HYPO71: A computer program for determining hypocenter, magnitude, and first motion pattern of local earthquakes.* US

Department of the Interior, Geological Survey, National Center for determining hypocenter, magnitude, and first motion pattern of local earthquakes. doi: https://doi.org/10.3133/ofr75311

Li, J., Liu, G., Qiao, X., Xiong, W., Liu, D., Sun, J., ... others (2019). Rupture characteristics of the 25 November 2016 Aketao earthquake (Mw 6.6) in eastern Pamir revealed by GPS and teleseismic data. In *Earthquakes and Multi-hazards Around the Pacific Rim, Vol. II* (pp. 49–61). Springer.

Li, T., Schoenbohm, L. M., Chen, J., Yuan, Z., Feng, W., Li, W., ... others (2019). Cumulative and Coseismic (During the 2016 Mw 6.6 Aketao Earthquake) Deformation of the Dextral-Slip Muji Fault, Northeastern Pamir Orogen. *Tectonics*, *38*(11), 3975–3989.

Manga, M., Beresnev, I., Brodsky, E. E., Elkhoury, J. E., Elsworth, D., Ingebritsen, S. E., ... Wang, C.-Y. (2012). Changes in permeability caused by transient stresses: Field observations, experiments, and mechanisms. *Reviews of Geophysics*, *50*(2). Retrieved from `https://agupubs.onlinelibrary.wiley.com/doi/abs/10.1029/2011RG000382` doi: https://doi.org/10.1029/2011RG000382

Metzger, S., Ischuk, A., Deng, Z., Ratschbacher, L., Perry, M., Kufner, S.-K., ... Moreno, M. (2020). Dense GNSS profiles across the northwestern tip of the India-Asia collision zone: Triggered slip and westward flow of the Peter the First Range, Pamir, into the Tajik Depression. *Tectonics*, *39*(2), e2019TC005797.

Metzger, S., Schurr, B., Ratschbacher, L., Sudhaus, H., Kufner, S.-K., Schöne, T., ... Bendick, R. (2017). The 2015 mw7. 2 Sarez strike-slip Earthquake in the Pamir interior: Response to the underthrusting of India's western promontory. *Tectonics*, *36*(11), 2407–2421.

Michael, A. J. (1984). Determination of stress from slip data: faults and folds. *Journal of Geophysical Research: Solid Earth*, *89*(B13), 11517–11526.

Michael, A. J. (1987). Use of focal mechanisms to determine stress: a control study. *Journal of Geophysical Research: Solid Earth*, *92*(B1), 357–368.

Miller, S. A. (2020). Aftershocks are fluid-driven and decay rates controlled by permeability dynamics. *Nature Communications*, *11*(1), 5787. doi: 10.1038/s41467-020-19590-3

Miller, S. A., & Nur, A. (2000). Permeability as a toggle switch in fluid-controlled crustal processes. *Earth and Planetary Science Letters*, *183*(1-2), 133–146.

Morishita, Y., Lazecky, M., Wright, T. J., Weiss, J. R., Elliott, J. R., & Hooper, A. (2020). LiCSBAS: An open-source InSAR time series analysis package integrated with the LiCSAR automated Sentinel-1 InSAR processor. *Remote Sensing*, *12*(3), 424.

Nábělek, J., & Xia, G. (1995). Moment-tensor analysis using regional data: Application to the 25 March, 1993, Scotts Mills, Oregon, Earthquake. *Geophysical Research Letters*, *22*(1), 13–16.

Nöth, L. (1932). *Geologische Untersuchungen im nordwestlichen Pamirgebiet und mittleren Transalai*. Verlag Dietrich Reimer, Ernst Vohsen.

Okada, Y. (1985). Surface deformation due to shear and tensile faults in a half-space. *Bulletin of the Seismological Society of America*, *75*(4), 1135–1154.

Perry, M., Kakar, N., Ischuk, A., Metzger, S., Bendick, R., Molnar, P., & Mohadjer, S. (2019). Little geodetic evidence for localized Indian subduction in the Pamir-Hindu Kush of Central Asia. *Geophysical Research Letters*, *46*(1), 109–118.

PMP International (Tajikistan). (2005). Tajikistan National Seismic Network [Computer software manual]. doi: doi:10.7914/SN/TJ

Pozzi, J.-P., & Feinberg, H. (1991). Paleomagnetism in the Tajikistan: Continental shortening of European margin in the Pamirs during Indian Eurasian collision. *Earth and Planetary Science Letters*, *103*(1-4), 365–378.

Qiao, X., Wang, Q., Yang, S., Li, J., Zou, R., & Ding, K. (2015). The 2008 Nura Mw6. 7 earthquake: A shallow rupture on the Main Pamir Thrust revealed by GPS and InSAR. *Geodesy and Geodynamics*, *6*(2), 91–100. doi: 10.1016/j.geog.2015.01.005

Rice, J. R., & Cleary, M. P. (1976). Some basic stress diffusion solutions for fluid-saturated elastic porous media with compressible constituents. *Reviews of Geophysics*, *14*(2), 227–241.

Robinson, A. C. (2009). Geologic offsets across the northern Karakorum fault: Implications for its role and terrane correlations in the western Himalayan-Tibetan orogen. *Earth and Planetary Science Letters*, *279*(1-2), 123–130.

Robinson, A. C., Yin, A., Manning, C. E., Harrison, T. M., Zhang, S.-H., & Wang,

X.-F. (2004). Tectonic evolution of the northeastern Pamir: Constraints from the northern portion of the Cenozoic Kongur Shan extensional system, western China. *Geological Society of America Bulletin*, *116*(7-8), 953–973.

Robinson, A. C., Yin, A., Manning, C. E., Harrison, T. M., Zhang, S.-H., & Wang, X.-F. (2007). Cenozoic evolution of the eastern Pamir: Implications for strain-accommodation mechanisms at the western end of the Himalayan-Tibetan orogen. *Geological Society of America Bulletin*, *119*(7-8), 882–896.

Rutte, D., Ratschbacher, L., Schneider, S., Stübner, K., Stearns, M. A., Gulzar, M. A., & Hacker, B. R. (2017). Building the Pamir-Tibetan Plateau—Crustal stacking, extensional collapse, and lateral extrusion in the Central Pamir: 1. Geometry and kinematics. *Tectonics*, *36*(3), 342–384.

Ryder, I., Bürgmann, R., & Fielding, E. (2012). Static stress interactions in extensional earthquake sequences: An example from the south lunggar rift, tibet. *Journal of Geophysical Research: Solid Earth*, *117*(B9). Retrieved from `https://agupubs.onlinelibrary.wiley.com/doi/abs/10.1029/2012JB009365` doi: https://doi.org/10.1029/2012JB009365

Sangha, S., Peltzer, G., Zhang, A., Meng, L., Liang, C., Lundgren, P., & Fielding, E. (2017). Fault geometry of 2015, Mw7. 2 Murghab, Tajikistan earthquake controls rupture propagation: Insights from InSAR and seismological data. *Earth and Planetary Science Letters*, *462*, 132–141.

Sass, P., Ritter, O., Ratschbacher, L., Tympel, J., Matiukov, V., Rybin, A., & Batalev, V. Y. (2014). Resistivity structure underneath the Pamir and southern Tian Shan. *Geophysical Journal International*, *198*(1), 564–579.

Schneider, F., Yuan, X., Schurr, B., Mechie, J., Sippl, C., Haberland, C., ... others (2013). Seismic imaging of subducting continental lower crust beneath the Pamir. *Earth and Planetary Science Letters*, *375*, 101–112.

Schurr, B., Moreno, M., Tréhu, A. M., Bedford, J., Kummerow, J., Li, S., & Oncken, O. (2020). Forming a Mogi doughnut in the years prior to and immediately before the 2014 M8.1 Iquique, northern Chile, earthquake. *Geophysical Research Letters*, *47*(16), e2020GL088351.

Schurr, B., Ratschbacher, L., Sippl, C., Gloaguen, R., Yuan, X., & Mechie, J. (2014). Seismotectonics of the Pamir. *Tectonics*, *33*(8), 1501–1518.

SEISDMC. (2021). Data management centre of the China National Seismic Net-

work at the Institute of Geophysics. *China Earthquake Administration*. doi: 10 .11998/SeisDmc/SN

Shapiro, S. A., Huenges, E., & Borm, G. (1997). Estimating the crust permeability from fluid-injection-induced seismic emission at the KTB site. *Geophysical Journal International*, *131*(2), F15–F18. doi: 10.1111/j.1365-246x.1997 .tb01215.x

Shapiro, S. A., Patzig, R., Rothert, E., & Rindschwentner, J. (2003). Triggering of seismicity by pore-pressure perturbations: Permeability-related signatures of the phenomenon. In *Thermo-hydro-mechanical coupling in fractured rock* (pp. 1051–1066). Birkhäuser Basel. doi: 10.1007/978-3-0348-8083-1_16

Sibson, R. (1992). Implications of fault-valve behaviour for rupture nucleation and recurrence. *Tectonophysics*, *211*(1-4), 283–293.

Sippl, C., Ratschbacher, L., Schurr, B., Krumbiegel, C., Rui, H., Pingren, L., & Abdybachaev, U. (2014). The 2008 Nura earthquake sequence at the Pamir-Tian Shan collision zone, southern Kyrgyzstan. *Tectonics*, *33*(12), 2382–2399.

Sippl, C., Schurr, B., Tympel, J., Angiboust, S., Mechie, J., Yuan, X., ... others (2013). Deep burial of Asian continental crust beneath the Pamir imaged with local earthquake tomography. *Earth and Planetary Science Letters*, *384*, 165–177.

Sippl, C., Schurr, B., Yuan, X., Mechie, J., Schneider, F., Gadoev, M., ... others (2013). Geometry of the Pamir-Hindu Kush intermediate-depth earthquake zone from local seismic data. *Journal of Geophysical Research: Solid Earth*, *118*(4), 1438–1457.

Sobel, E. R., Schoenbohm, L. M., Chen, J., Thiede, R., Stockli, D. F., Sudo, M., & Strecker, M. R. (2011). Late Miocene–Pliocene deceleration of dextral slip between Pamir and Tarim: Implications for Pamir orogenesis. *Earth and Planetary Science Letters*, *304*(3-4), 369–378.

Stein, R. S. (1999). The role of stress transfer in earthquake occurrence. *Nature*, *402*(6762), 605–609.

Strecker, M., Frisch, W., Hamburger, M., Ratschbacher, L., Semiletkin, S., Zamoruyev, A., & Sturchio, N. (1995). Quaternary deformation in the eastern Pamirs, Tadzhikistan and Kyrgyzstan. *Tectonics*, *14*(5), 1061–1079.

Strom, A. (2014). Sarez Lake problem: ensuring long-term safety. In *Landslide Sci-*

*ence for a Safer Geoenvironment* (pp. 633–639). Springer.

Stübner, K., Ratschbacher, L., Rutte, D., Stanek, K., Minaev, V., Wiesinger, M., ... members, P. T. (2013). The giant Shakhdara migmatitic gneiss dome, Pamir, India-Asia collision zone: 1. Geometry and kinematics. *Tectonics*, *32*(4), 948–979.

Tanaka, S., Ohtake, M., & Sato, H. (2002). Evidence for tidal triggering of earthquakes as revealed from statistical analysis of global data. *Journal of Geophysical Research: Solid Earth*, *107*(B10), ESE–1.

Teshebaeva, K., Sudhaus, H., Echtler, H., Schurr, B., & Roessner, S. (2014). Strain partitioning at the eastern Pamir-Alai revealed through SAR data analysis of the 2008 Nura earthquake. *Geophysical Journal International*, *198*(2), 760–774.

Thiede, R. C., Sobel, E. R., Chen, J., Schoenbohm, L. M., Stockli, D. F., Sudo, M., & Strecker, M. R. (2013). Late Cenozoic extension and crustal doming in the India-Eurasia collision zone: New thermochronologic constraints from the NE Chinese Pamir. *Tectonics*, *32*(3), 763–779.

Thomas, J.-C., Chauvin, A., Gapais, D., Bazhenov, M., Perroud, H., Cobbold, P., & Burtman, V. (1994). Paleomagnetic evidence for Cenozoic block rotations in the Tadjik depression (Central Asia). *Journal of Geophysical Research: Solid Earth*, *99*(B8), 15141–15160.

Thurber, C. H. (1983). Earthquake locations and three-dimensional crustal structure in the Coyote Lake area, central California. *Journal of Geophysical Research: Solid Earth*, *88*(B10), 8226–8236.

Toda, S., & Stein, R. S. (2020). Long-and short-term stress interaction of the 2019 Ridgecrest sequence and Coulomb-based earthquake forecasts. *Bulletin of the Seismological Society of America*, *110*(4), 1765–1780.

Toda, S., Stein, R. S., Reasenberg, P. A., Dieterich, J. H., & Yoshida, A. (1998). Stress transferred by the 1995 Mw=6.9 Kobe, Japan, shock: Effect on aftershocks and future earthquake probabilities. *Journal of Geophysical Research: Solid Earth*, *103*(B10), 24543–24565.

Waldhauser, F., & Ellsworth, W. L. (2000). A double-difference earthquake location algorithm: Method and application to the northern Hayward fault, California. *Bulletin of the Seismological Society of America*, *90*(6), 1353–1368.

Wang, R., Lorenzo-Martin, F., & Roth, F. (2006). PSGRN/PSCMP—a new code for calculating co-and post-seismic deformation, geoid and gravity changes based on the viscoelastic-gravitational dislocation theory. *Computers & Geosciences*, *32*(4), 527–541.

Wells, D. L., & Coppersmith, K. J. (1994). New empirical relationships among magnitude, rupture length, rupture width, rupture area, and surface displacement. *Bulletin of the seismological Society of America*, *84*(4), 974–1002.

Wessel, P., Smith, W. H., Scharroo, R., Luis, J., & Wobbe, F. (2013). Generic mapping tools: improved version released. *Eos, Transactions American Geophysical Union*, *94*(45), 409–410.

Woessner, J., & Wiemer, S. (2005). Assessing the quality of earthquake catalogues: Estimating the magnitude of completeness and its uncertainty. *Bulletin of the Seismological Society of America*, *95*(2), 684–698. doi: 10.1785/0120040007

Worthington, J. R., Ratschbacher, L., Stübner, K., Khan, J., Malz, N., Schneider, S., ... others (2020). The Alichur dome, South Pamir, western India–Asia collisional zone: Detailing the Neogene Shakhdara–Alichur syn-collisional gneiss-dome complex and connection to lithospheric processes. *Tectonics*, *39*(1), e2019TC005735.

Yamashita, T. (1999). Pore creation due to fault slip in a fluid-permeated fault zone and its effect on seismicity: Generation mechanism of earthquake swarm. In *Seismicity patterns, their statistical significance and physical meaning* (pp. 625–647). Birkhäuser Basel. doi: 10.1007/978-3-0348-8677-2_19

Yu, C., Li, Z., Penna, N. T., & Crippa, P. (2018). Generic atmospheric correction model for Interferometric Synthetic Aperture Radar observations. *Journal of Geophysical Research: Solid Earth*, *123*(10), 9202–9222.

Yuan, X., Schurr, B., Bloch, W., Xu, Q., & Zhao, J. (2018). East Pamir seismic network. *GFZ Data services*. doi: 10.14470/3U7560589977

Yuan, X., Schurr, B., Kufner, S.-K., & Bloch, W. (2018). Sarez Pamir aftershock seismic network. *GFZ Data services*. doi: 10.14470/4U7561589984

Yushin, I., Sass, M., Karapetov, S., Altukhov, S., Teplov, I., Raeakov, C., ... Davidchenko, A. (1964). *1: 200,000 maps of the Tajik SSR*. Nedra, Moscow: Russian Geological Research Institute.

Zhou, Y., He, J., Oimahmadov, I., Gadoev, M., Pan, Z., Wang, W., ... Rajabov,

N. (2016). Present-day crustal motion around the Pamir Plateau from GPS measurements. *Gondwana Research*, *35*, 144–154.

Zubovich, A. V., Schöne, T., Metzger, S., Mosienko, O., Mukhamediev, S., Sharshebaev, A., & Zech, C. (2016). Tectonic interaction between the Pamir and Tien Shan observed by GPS. *Tectonics*, *35*(2), 283–292.

Zubovich, A. V., Wang, X.-q., Scherba, Y. G., Schelochkov, G. G., Reilinger, R., Reigber, C., ... Beisenbaev, R. T. (2010). GPS velocity field for the Tien Shan and surrounding regions. *Tectonics*, *29*(6), TC6014. Retrieved from `https://agupubs.onlinelibrary.wiley.com/doi/abs/10.1029/2010TC002772` doi: https://doi.org/10.1029/2010TC002772

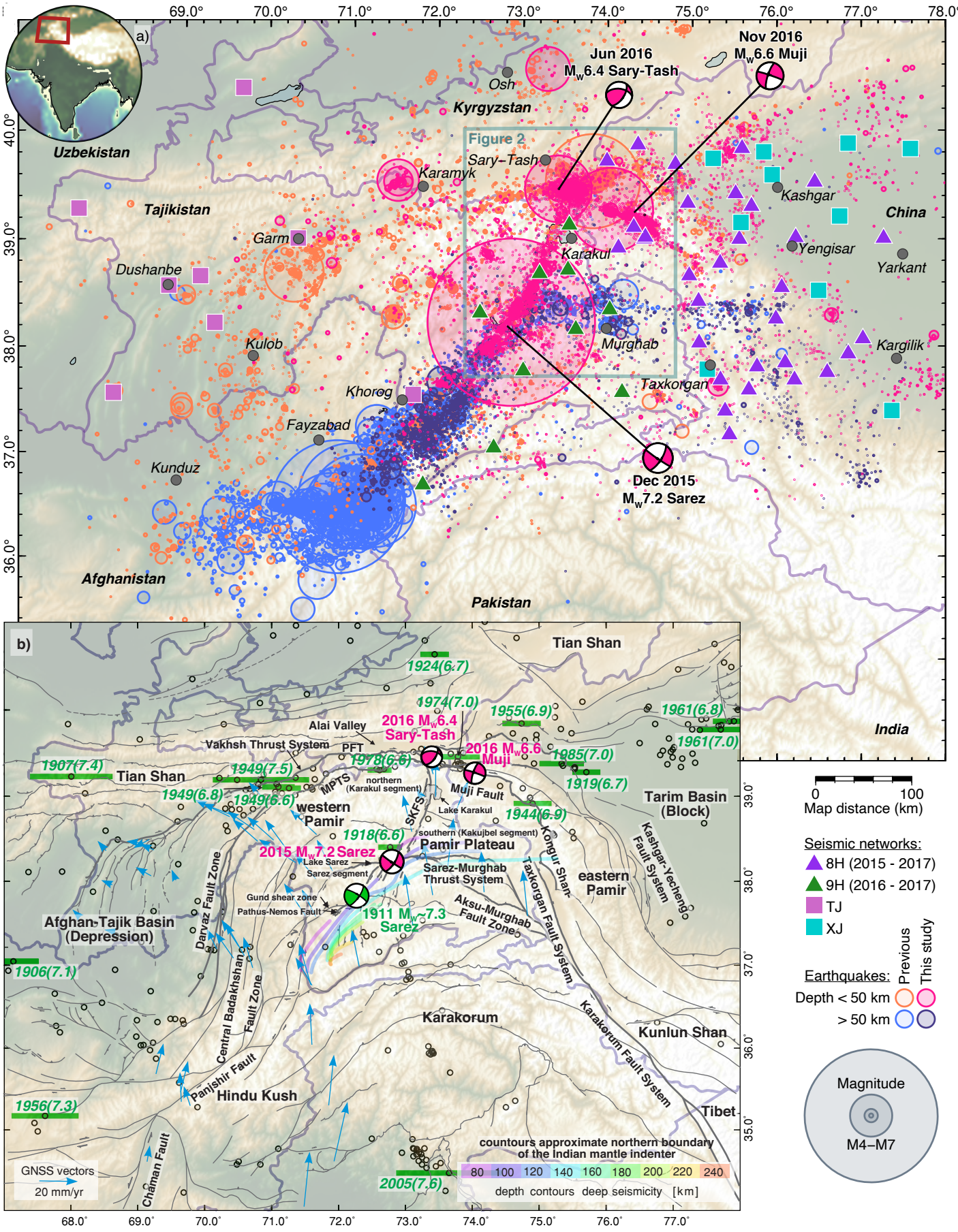
a)
Uzbekistan
Tajikistan
Afghanistan
Pakistan
China
India
Osh
Kyrgyzstan
Sary-Tash
Karamyk
Garm
Dushanbe
Kulob
Khorog
Fayzabad
Kunduz
Karakul
Murghab
Taxkorgan
Yengisar
Kashgar
Yarkant
Kargilik
Figure 2
Jun 2016
$M_w$6.4 Sary-Tash
Nov 2016
$M_w$6.6 Muji
Dec 2015
$M_w$7.2 Sarez
69.0°
70.0°
71.0°
72.0°
73.0°
74.0°
75.0°
76.0°
77.0°
78.0°
40.0°
39.0°
38.0°
37.0°
36.0°
b)
Tian Shan
Alai Valley
Vakhsh Thrust System
PFT
MPTS
northern (Karakul segment)
western Pamir
Pamir Plateau
southern (Kakujbel segment)
Lake Karakul
Muji Fault
SKFS
Kongur Shan
Taxkorgan Fault System
Kashgar-Yechengo Fault System
eastern Pamir
Tarim Basin (Block)
Lake Sarez
Sarez segment
Sarez-Murghab Thrust System
Gund shear zone
Pathus-Nemos Fault
Aksu-Murghab Fault Zone
Darvaz Fault Zone
Afghan-Tajik Basin (Depression)
Central Badakhshan Fault Zone
Panjshir Fault
Hindu Kush
Chaman Fault
Karakorum
Karakorum Fault System
Kunlun Shan
Tibet
1924(6.7)
1974(7.0)
2016 $M_w$6.4 Sary-Tash
1955(6.9)
1961(6.8)
1961(7.0)
2016 $M_w$6.6 Muji
1985(7.0)
1907(7.4)
1978(6.6)
1949(7.5)
1919(6.7)
1949(6.8)
1949(6.6)
1944(6.9)
1918(6.6)
2015 $M_w$7.2 Sarez
1911 $M_w$~7.3 Sarez
1906(7.1)
1956(7.3)
2005(7.6)
countours approximate northern boundary of the Indian mantle indenter
80 100 120 140 160 180 200 220 240
depth contours deep seismicity [km]
GNSS vectors
20 mm/yr
68.0°
69.0°
70.0°
71.0°
72.0°
73.0°
74.0°
75.0°
76.0°
77.0°
39.0°
38.0°
37.0°
36.0°
35.0°
0
100
Map distance (km)
Seismic networks:
8H (2015 - 2017)
9H (2016 - 2017)
TJ
XJ
Earthquakes:
Previous
This study
Depth < 50 km
> 50 km
Magnitude
M4–M7

**Figure 1.** (a) Location of the study area, seismic stations, seismicity from this and previous (Schurr et al., 2014; Kufner et al., 2017, 2018) studies, and moment tensors of the three largest earthquakes of the sequence. Crustal seismicity (depth $< 50$ km) delineates the active fault zones. Intermediate depth seismicity (depth $> 50$ km) indicates subduction of Indian lithosphere beneath the Hindu Kush (Kufner et al., 2017, 2021) and delamination of Asian lithosphere beneath the Pamir (Sippl, Schurr, Yuan, et al., 2013; Bloch et al., 2021). (b) Cenozoic fault map with the neotectonic faults discussed in the text highlighted and named. Instrumentally recorded earthquakes since 1900 with $M > 5.5$ as black circles and $M > 6.5$ as green bars (Bondár et al., 2015; Di Giacomo et al., 2018; ISC, 2021) indicating approximate rupture length (Wells & Coppersmith, 1994). Focal mechanism of the 1911 Sarez earthquake is from Kulikova et al. (2016) and its location follows Elliott et al. (2020). Depth contours of intermediate-depth seismicity are from Schurr et al. (2014). Global Navigation Satellite System (GNSS) displacement rates from the Pamir Plateau and its western foreland are from Perry et al. (2019). MPTS: Main Pamir Thrust System. PFT: Pamir Frontal Thrust. SKFS: Sarez-Karakul Fault System.

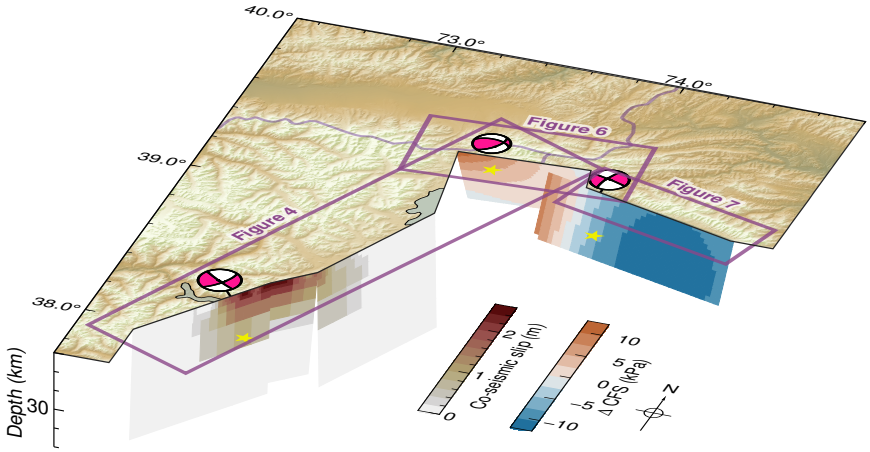


**Figure 2.** Perspective view onto the three activated fault segments, with slip of the Sarez earthquake (Figure 4) and thereby imposed static change in Coulomb Failure Stress ($\Delta$CFS) on the Sary-Tash (Figure 6) and Muji (Figure 7) earthquake faults. Stars: earthquake hypocenters. The Coulomb Failure Stress change on the fault planes of the future large earthquakes is small ($\sim$5 kPa) or even negative ($\sim$-7 kPa).

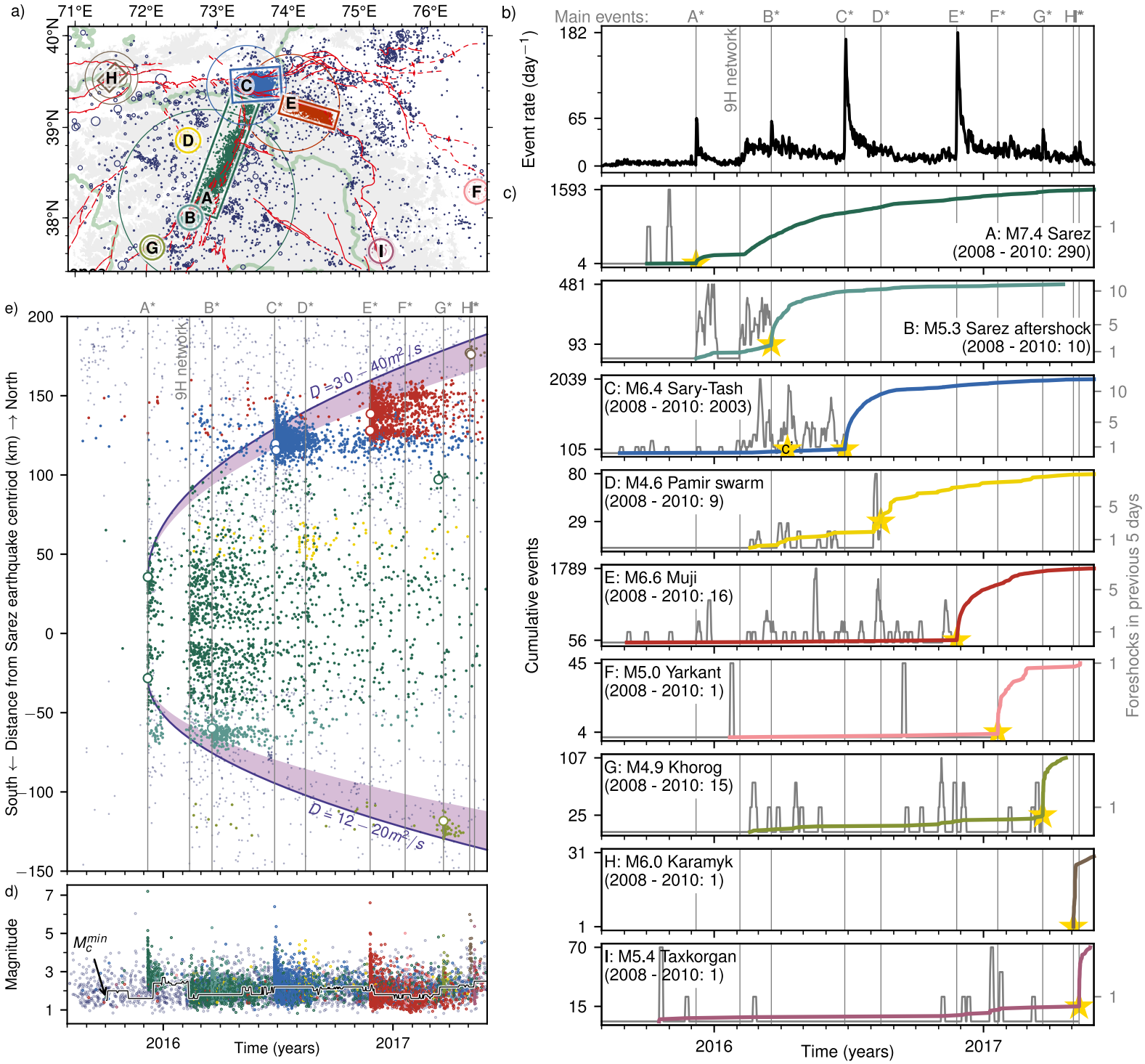
a)
71°E
72°E
73°E
74°E
75°E
76°E
40°N
39°N
38°N
H
C
E
D
A
B
F
G
I
b)
Main events:
A*
B*
C*
D*
E*
F*
G*
H*
Event rate (day$^{-1}$)
182
65
0
9H network
c)
Cumulative events
1593
4
A: M7.4 Sarez
(2008 - 2010: 290)
481
93
B: M5.3 Sarez aftershock
(2008 - 2010: 10)
2039
105
C: M6.4 Sary-Tash
(2008 - 2010: 2003)
80
29
D: M4.6 Pamir swarm
(2008 - 2010: 9)
1789
56
E: M6.6 Muji
(2008 - 2010: 16)
45
4
F: M5.0 Yarkant
(2008 - 2010: 1)
107
25
G: M4.9 Khorog
(2008 - 2010: 15)
31
1
H: M6.0 Karamyk
(2008 - 2010: 1)
70
15
I: M5.4 Taxkorgan
(2008 - 2010: 1)
10
5
1
Foreshocks in previous 5 days
2016
Time (years)
2017
e)
A*
B*
C*
D*
E*
F*
G*
H*
9H network
200
150
100
50
0
−50
−100
−150
South ← Distance from Sarez earthquake centriod (km) → North
D = 30 – 40m$^2$/s
D = 12 – 20m$^2$/s
d)
Magnitude
7
5
3
1
$M_c^{min}$
2016
Time (years)
2017

**Figure 3.** Spatio-temporal evolution of seismic activity. (a) Spatial definitions of sequences ($A$ to $I$) with earthquakes color-coded as in the other subfigures and Figure 8. (b) Seismic event rate over time. (c) Cumulative event number inside each sequence (colored) and 5-day moving window event number before the mainshock for each sequence (gray); event with largest magnitude in sequence is marked with a star and labeled on top. The number in the sequence of the strongest and the last event is labeled on the left. Cumulative event number from 2008 to 2010 for the specific region in parenthesis from Schurr et al. (2014). For aftershock event rate, see Figure S13. (d) Magnitude over time with time variable minimum magnitude of completeness ($M_c^{min}$). (e) Spatio-temporal distribution of the seismic events with respect to the $M_W$ 7.2 Sarez earthquake centroid. $M_W > 4.8$ events are highlighted as larger circles. The activation of the mainshock rupture planes mimics the diffusion equation 8 with scaling constant $D$ (Figure S16). Most of the future mainshock volumes show foreshock activity, but foreshock activity is independent of mainshocks on other faults.

**Table 1.** Source parameters and failure stresses of the large and moderate earthquakes for which a moment tensor is available. Strike, dip and rake of our preferred fault plane. # denotes our moment tensors shown in Figure 8; Sequence (Seq.) denotes the studied earthquake sequence, defined in Figure 3; * denotes the largest earthquake of the sequence. Depth is centroid depth, except for the three largest mainshocks, for which we report hypocentral depths. The change in Coulomb failure stress (ΔCFS) is due to all previous earthquakes. For c' and C*, ΔCFS without possible creep on the SKFS (Figure 5) is given in brackets. Large negative ΔCFS in parenthesis are artifacts of the too coarse fault-slip models that lack small scale slip heterogeneities.

| # | Seq. | Time | $M_W$ | Lon. (°E) | Lat. (°N) | Depth (km) | Stike/Dip/Rake (°) | ΔCFS (kPa) |
|---|---|---|---|---|---|---|---|---|
| | A* | 2015-12-07 07:50:04 | 7.2[a] | 72.853 | 38.223 | 0.9 | 214/83/8[a] | $0^{+0}_{-0}$ |
| 1 | A | 2015-12-07 10:34:22 | 4.4 | 72.904 | 38.289 | 9.0 | 26/81/24 | $(-425^{+345}_{-295})$ |
| 2 | A | 2015-12-07 15:23:56 | 4.6 | 73.225 | 38.719 | 4.0 | 198/40/344 | $(-189^{+122}_{-169})$ |
| 3 | B | 2015-12-27 23:05:28 | 4.2 | 72.697 | 38.069 | 6.0 | 181/40/234 | $+27^{+52}_{-34}$ |
| 4 | A | 2016-01-13 21:37:37 | 4.8 | 73.322 | 38.742 | 9.0 | 225/40/338 | $+102^{+65}_{-38}$ |
| 5 | B* | 2016-03-18 16:11:00 | 5.3 | 72.618 | 38.003 | 4.0 | 219/68/5 | $+132^{+70}_{-56}$ |
| 6 | B | 2016-03-21 05:32:27 | 4.1 | 72.581 | 38.002 | 4.0 | 230/38/325 | $(-306^{+124}_{-108})$ |
| 7 | c' | 2016-04-09 16:19:33 | 4.4 | 73.502 | 39.428 | 9.0 | 79/50/157 | $+4^{+2}_{-2}$ $[+8^{+3}_{-3}]^d$ |
| | C* | 2016-06-26 11:17:08 | 6.4[a] | 73.411 | 39.462 | 11.9 | 266/67/126[b] | $+4^{+4}_{-3}$ $[+3^{+4}_{-5}]^d$ |
| 8 | C | 2016-06-27 06:25:37 | 4.6 | 73.463 | 39.438 | 12.0 | 278/55/120 | $(-434^{+198}_{-270})$ |
| 9 | C | 2016-06-27 07:34:13 | 4.3 | 73.657 | 39.447 | 6.0 | 123/37/194 | $+499^{+160}_{-138}$ |
| 10 | C | 2016-06-27 19:28:49 | 4.8 | 73.544 | 39.441 | 15.0 | 265/33/93 | $(-2007^{+516}_{-671})$ |
| 11 | C | 2016-06-28 12:43:16 | 4.7 | 73.499 | 39.456 | 15.0 | 292/28/182 | $(-596^{+354}_{-340})$ |
| 12 | C | 2016-06-28 21:38:04 | 5.4 | 73.412 | 39.440 | 15.0 | 91/80/163 | $+111^{+251}_{-288}$ |
| 13 | C | 2016-06-29 08:08:14 | 4.5 | 73.471 | 39.443 | 12.0 | 287/52/139 | $(-791^{+225}_{-249})$ |
| 14 | A | 2016-06-30 07:09:43 | 4.2 | 72.930 | 38.426 | 18.0 | 217/82/320 | $(-1038^{+348}_{-385})$ |
| 15 | C | 2016-07-01 11:01:14 | 4.0 | 73.733 | 39.449 | 6.0 | 134/33/222 | $+335^{+91}_{-110}$ |
| 16 | C | 2016-07-04 02:24:20 | 4.4 | 73.525 | 39.446 | 9.0 | 308/81/186 | $-9^{+96}_{-120}$ |
| 17 | A | 2016-07-08 12:10:25 | 4.1 | 72.840 | 38.085 | 4.0 | 49/88/306 | $(-82^{+221}_{-223})$ |
| 18 | C | 2016-07-21 05:29:20 | 4.5 | 73.527 | 39.450 | 6.0 | 238/81/73 | $(-393^{+111}_{-125})$ |
| 19 | D | 2016-08-04 21:34:41 | 4.1 | 72.568 | 38.877 | 4.0 | 352/69/263 | $+33^{+20}_{-14}$ |
| 20 | D | 2016-08-04 23:42:17 | 4.4 | 72.548 | 38.868 | 4.0 | 350/71/264 | $+10^{+18}_{-18}$ |
| 21 | D* | 2016-08-14 15:05:20 | 4.6 | 72.590 | 38.858 | 6.0 | 329/72/234 | $+18^{+13}_{-10}$ |
| 22 | D | 2016-08-14 15:11:39 | 4.2 | 72.584 | 38.838 | 4.0 | 22/66/287 | $+103^{+24}_{-26}$ |
| 23 | e' | 2016-11-25 14:18:59 | 5.0 | 74.034 | 39.267 | 15.0 | 291/68/173 | $-13^{+5}_{-9}$ |
| | E* | 2016-11-25 14:24:27 | 6.6[a] | 74.039 | 39.269 | 13.7 | 106/88/184[c] | $+59^{+157}_{-172}$ |
| 24 | E | 2016-11-25 19:46:19 | 4.2 | 74.295 | 39.198 | 6.0 | 292/77/192 | $(-2072^{+762}_{-784})$ |
| 25 | E | 2016-11-26 09:23:26 | 5.0 | 74.274 | 39.202 | 6.0 | 293/80/224 | $(-1175^{+501}_{-371})$ |
| 26 | E | 2016-12-19 10:57:33 | 4.4 | 74.047 | 39.256 | 15.0 | 290/59/160 | $(-540^{+522}_{-363})$ |
| 27 | F* | 2017-01-20 09:54:08 | 5.0 | 76.653 | 38.292 | 12.0 | 176/25/121 | $0^{+0}_{-0}$ |
| 28 | A | 2017-03-14 11:07:11 | 4.8 | 73.455 | 39.249 | 12.0 | 191/84/351 | $+23^{+19}_{-28}$ |
| 29 | G* | 2017-03-22 11:27:02 | 4.9 | 72.084 | 37.668 | 12.0 | 238/88/8 | $+12^{+4}_{-5}$ |
| 30 | H* | 2017-05-03 04:47:13 | 6.0 | 71.510 | 39.542 | 15.0 | 251/74/178 | $-3^{+1}_{-1}$ |
| 31 | H | 2017-05-05 05:09:35 | 5.7 | 71.514 | 39.532 | 12.0 | 237/48/115 | $(-1210^{+318}_{-430})$ |
| 32 | I* | 2017-05-10 21:58:21 | 5.4 | 75.305 | 37.627 | 6.0 | 317/60/247 | $+0^{+0}_{-0}$ |
| 33 | C | 2017-05-22 09:23:09 | 4.5 | 73.645 | 39.409 | 4.0 | 60/72/89 | $(-1356^{+348}_{-361})$ |

[a]NEIC; [b]He et al. (2018); [c]Bie et al. (2018); [d] without creep (Figure 5)

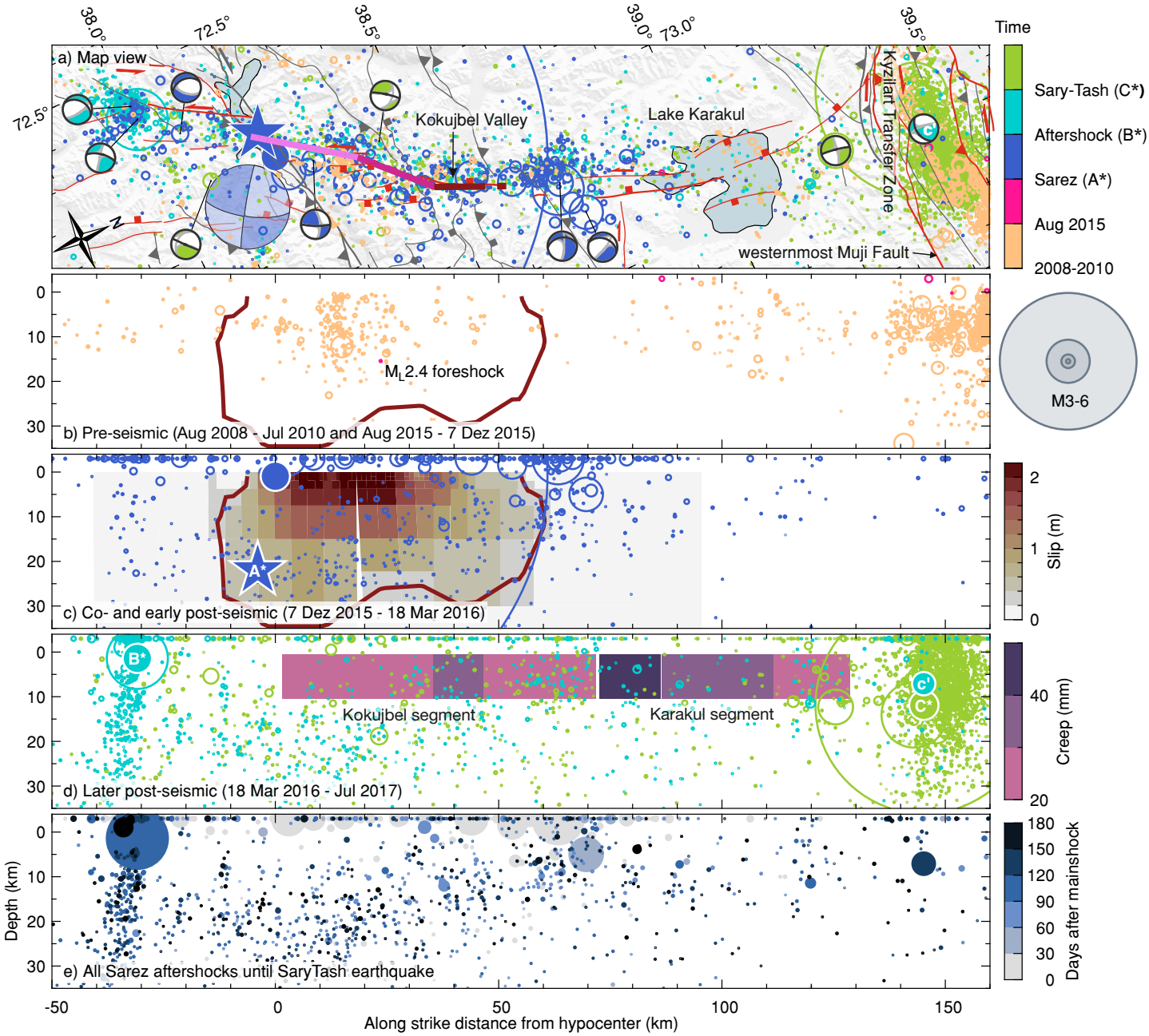
a) Map view
Kokujbel Valley
Lake Karakul
Kyzilart Transfer Zone
westernmost Muji Fault
Time
Sary-Tash (C*)
Aftershock (B*)
Sarez (A*)
Aug 2015
2008-2010
M3-6
M_L 2.4 foreshock
b) Pre-seismic (Aug 2008 - Jul 2010 and Aug 2015 - 7 Dez 2015)
c) Co- and early post-seismic (7 Dez 2015 - 18 Mar 2016)
Slip (m)
Kokujbel segment
Karakul segment
d) Later post-seismic (18 Mar 2016 - Jul 2017)
Creep (mm)
e) All Sarez aftershocks until SaryTash earthquake
Days after mainshock
Depth (km)
Along strike distance from hypocenter (km)

**Figure 4.** Time succession of seismicity and moment tensors of moderate earthquakes in the active part of the Sarez-Karakul Fault Zone; GEOFON focal mechanism of the mainshock (large beach ball); preferred hypocenter location by NEIC (star); 2008–2010 seismicity from Schurr et al. (2014). (a) Along-strike map view with the three segments of the co-seismic rupture highlighted (Metzger et al., 2017). Mapped Cenozoic structures in gray and neotectonic structures in red. Beach ball representation of moment tensors (Table 1) with preferred fault plane in black. (b–d) Along strike profiles. (b) Seismicity before the Sarez mainshock. 10% of maximum future slip contoured. (c) Early aftershock seismicity until aftershock $B^*$. Co-seismic slip from Metzger et al. (2017). (d) Later aftershock seismicity. Cumulative creep model as in Figure 4 between $A^*$ and $C^*$ (Table 1). (e) Time succession of the Sarez aftershocks until the Sary-Tash earthquake. The larger ($M \quad > 4$) earthquakes migrated away from the mainshock rupture. No significant immediate foreshock activity was detected for the Sarez earthquake. The rupture plane has been constantly active throughout 2008–2010. Aftershock seismicity skirts around the co-seismic slip patch.

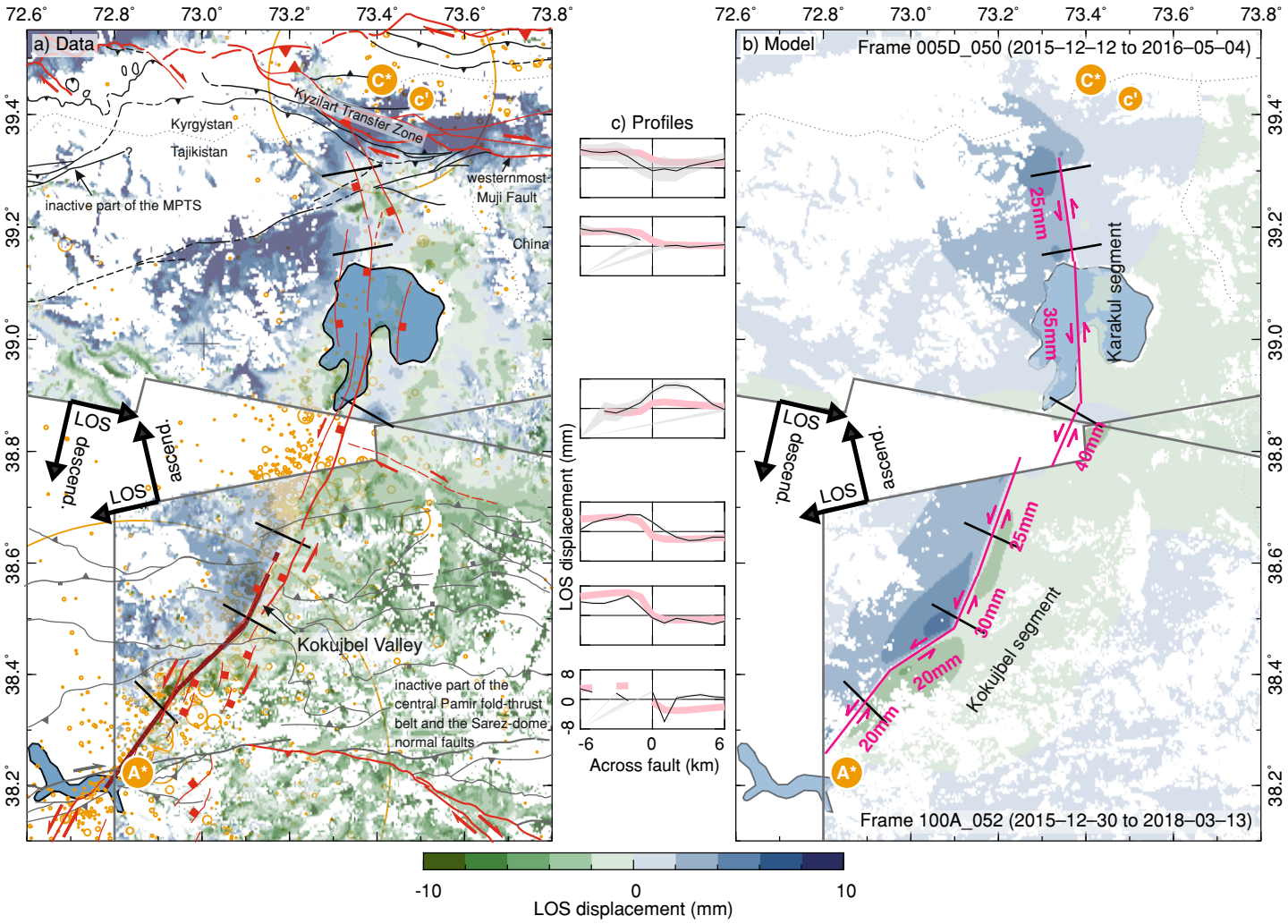
a) Data
b) Model
Frame 005D_050 (2015–12–12 to 2016–05–04)
Frame 100A_052 (2015–12–30 to 2018–03–13)
c) Profiles
Kyrgystan
Tajikistan
Kyzilart Transfer Zone
westernmost Muji Fault
China
inactive part of the MPTS
Kokujbel Valley
inactive part of the central Pamir fold-thrust belt and the Sarez-dome normal faults
Karakul segment
Kokujbel segment
LOS
ascend.
descend.
25mm
35mm
40mm
25mm
30mm
20mm
20mm
LOS displacement (mm)
Across fault (km)
-10
0
10
LOS displacement (mm)

**Figure 5.** Post-seismic displacement on the Sarez-Karakul Fault System. (a) InSAR displacement map derived from the displacement-rate map (Figure S5). Seismicity between $A*$ and $C*$, main- and foreshock hypocenters highlighted in orange. Mapped Cenozoic structures in gray and neotectonic structures in red. (b) Fault creep model and synthetic data. (c) Across-strike displacement profiles with data (black), nominal data uncertainty (gray), and model (pink). Displacement is accumulated in 202 days between events $A*$ and $C*$. LOS: line-of-sight vector. See Figure 4d for along-strike view of the creep model and Figure S10 for uncertainty in map view.

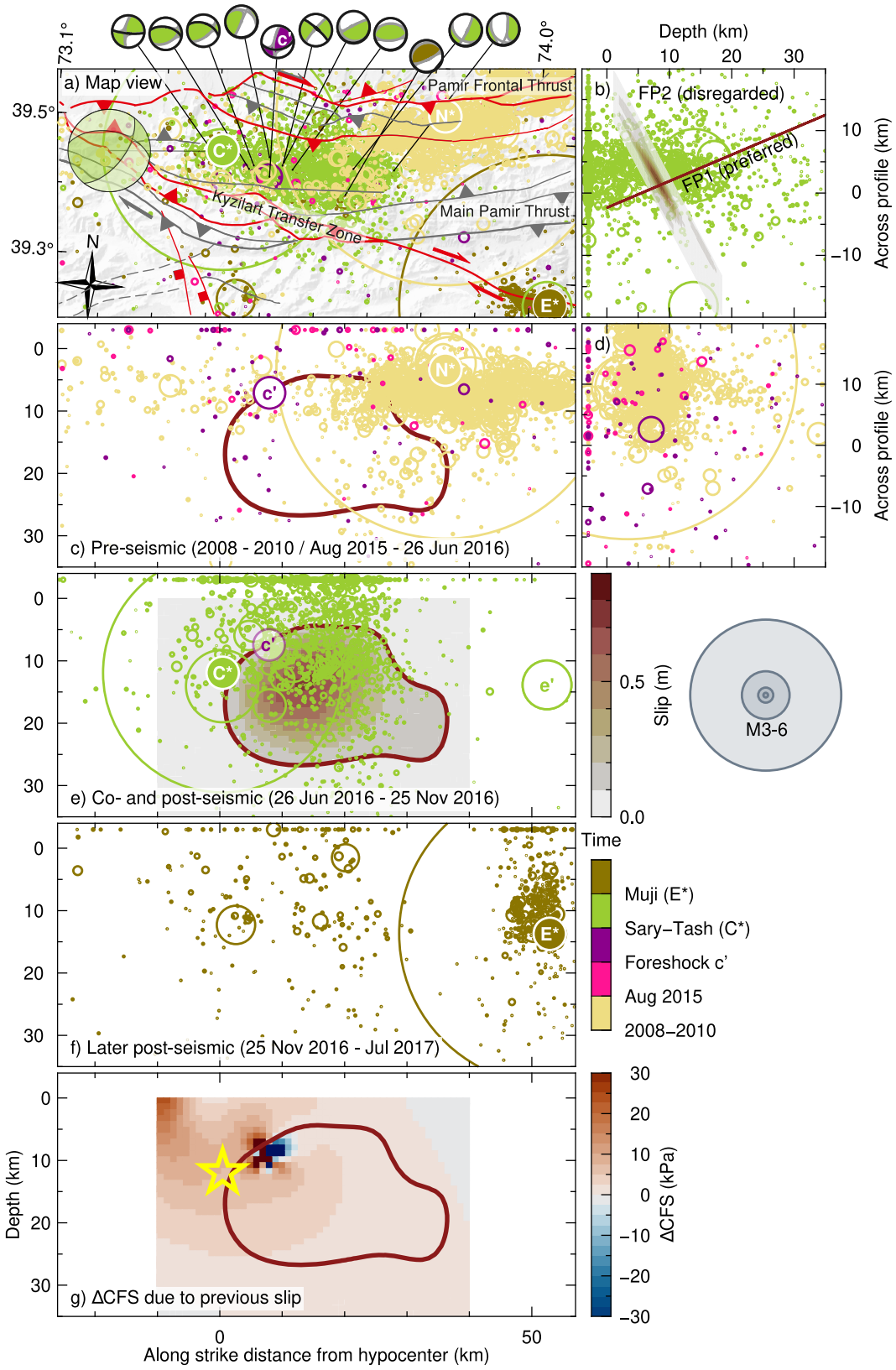
73.1°
74.0°
39.5°
39.3°
a) Map view
Pamir Frontal Thrust
Kyzylart Transfer Zone
Main Pamir Thrust
N
b)
Depth (km)
0
10
20
30
FP2 (disregarded)
FP1 (preferred)
Across profile (km)
c) Pre-seismic (2008 - 2010 / Aug 2015 - 26 Jun 2016)
d)
e) Co- and post-seismic (26 Jun 2016 - 25 Nov 2016)
Slip (m)
0.5
0.0
M3-6
Time
Muji (E*)
Sary−Tash (C*)
Foreshock c'
Aug 2015
2008−2010
f) Later post-seismic (25 Nov 2016 - Jul 2017)
g) ΔCFS due to previous slip
ΔCFS (kPa)
Depth (km)
Along strike distance from hypocenter (km)

**Figure 6.** Time succession of seismicity and moment tensors of moderate earthquakes in the active part of the Main Pamir Thrust System; GEOFON focal mechanism of the mainshock (large beach ball); 2008–2010 seismicity from Schurr et al. (2014); hypocenter of the 2008 Nura earthquake (*N**; Sippl et al., 2014) and fore- and mainshocks discussed in the text (*c'*, *C**, *e'*, *E**). (a) Along-strike map view. Mapped Cenozoic structures in gray and neotectonic structures in red. Beach ball representation of moment tensors (Table 1) with preferred fault plane in black. (b, d) Across-strike profiles. (c, e, f) Along-strike profiles. (b) Aftershock seismicity and the two possible fault planes of the mainshock (He et al., 2018). FP1 is preferred, because aftershock seismicity concentrates in the hanging wall. (c, d) Seismicity before the Sary-Tash mainshock; 10% of maximum future slip contoured. (e) Early aftershock seismicity until subsequent Muji mainshock *E**. Co-seismic slip from He et al. (2018). (f) Later aftershock seismicity and spatial configuration with the Muji earthquake (*E**). (g) $\Delta$CFS on the fault plane. Star marks the hypocenter. Foreshock activity left out the future rupture area and grossly concentrated around the future hypocenter since *c'*. Note the lesser depth extent of the Nura aftershock seismicity.

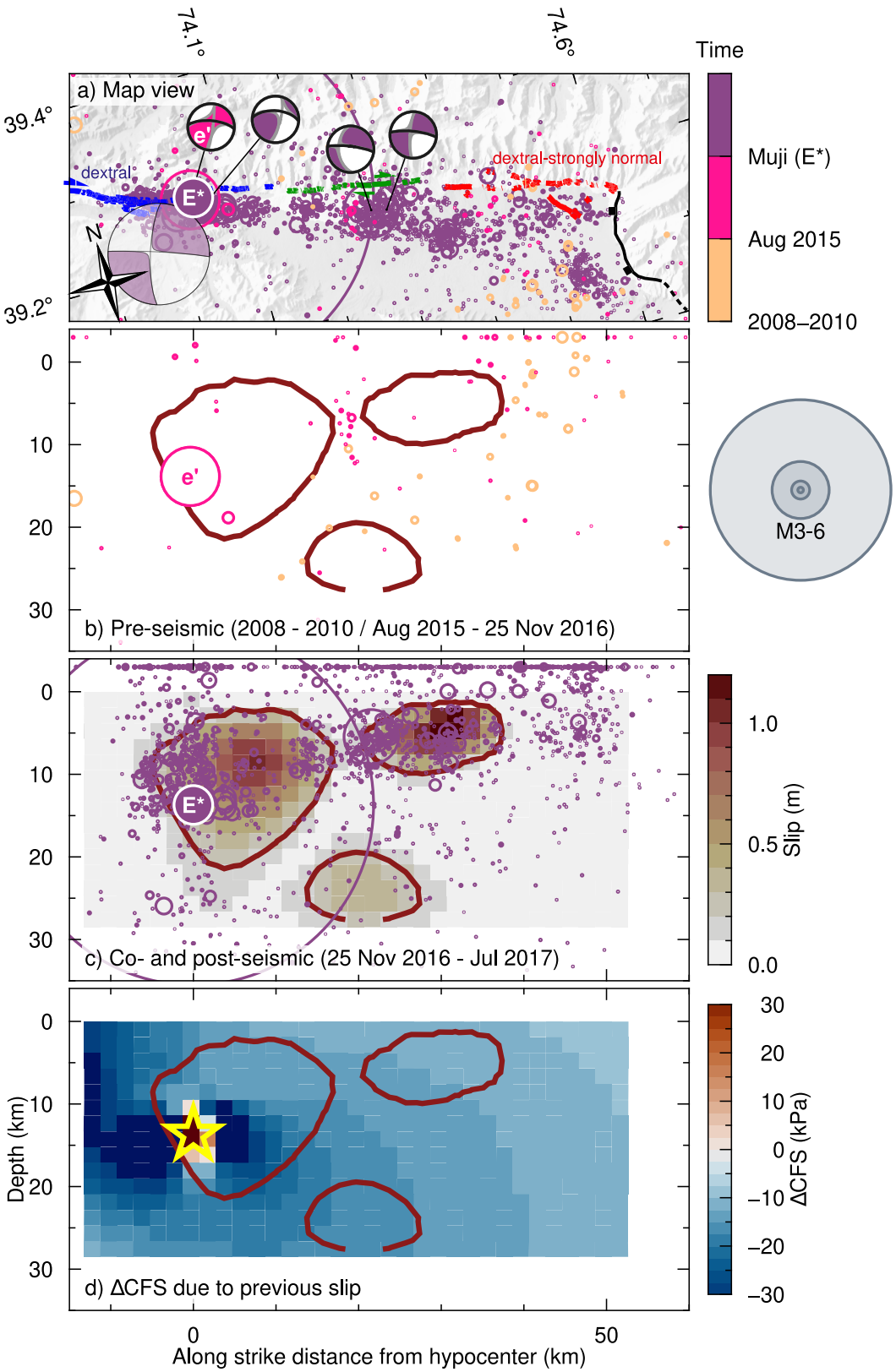
74.1°
74.6°
Time
a) Map view
39.4°
39.2°
e'
E*
dextral
dextral-strongly normal
N
Muji (E*)
Aug 2015
2008–2010
0
10
20
30
e'
M3-6
b) Pre-seismic (2008 - 2010 / Aug 2015 - 25 Nov 2016)
E*
1.0
0.5
0.0
Slip (m)
c) Co- and post-seismic (25 Nov 2016 - Jul 2017)
Depth (km)
30
20
10
0
−10
−20
−30
ΔCFS (kPa)
d) ΔCFS due to previous slip
0
50
Along strike distance from hypocenter (km)

**Figure 7.** Time succession of seismicity and moment tensors of moderate earthquakes in the active part of the Muji Fault; GEOFON focal mechanism (large beach ball); 2008–2010 seismicity from Schurr et al. (2014); fore- and mainshock hypocenters (*e'*, *E**). (a) Along-strike map view. Beach ball representation of moment tensors (Table 1) with preferred fault plane in black. Surface traces (blue, green, red) of the Muji-Fault earthquake and other faults modified from T. Li et al. (2019) (b, c) Along-strike profiles. (b) Seismicity before the mainshock; 10% of maximum future slip contoured, the lowermost slip patch is not resolved. (c) Aftershock seismicity and co-seismic slip model (Bie et al., 2018). (d) $\Delta$CFS model due to all previous earthquakes. Star: earthquake hypocenter. Foreshock activity left out the future rupture area. *e'* occurred 12 minutes before the mainshock, very close to the hypocenter location. Stress transfer from the previous earthquakes acted stabilizing on the fault plane.

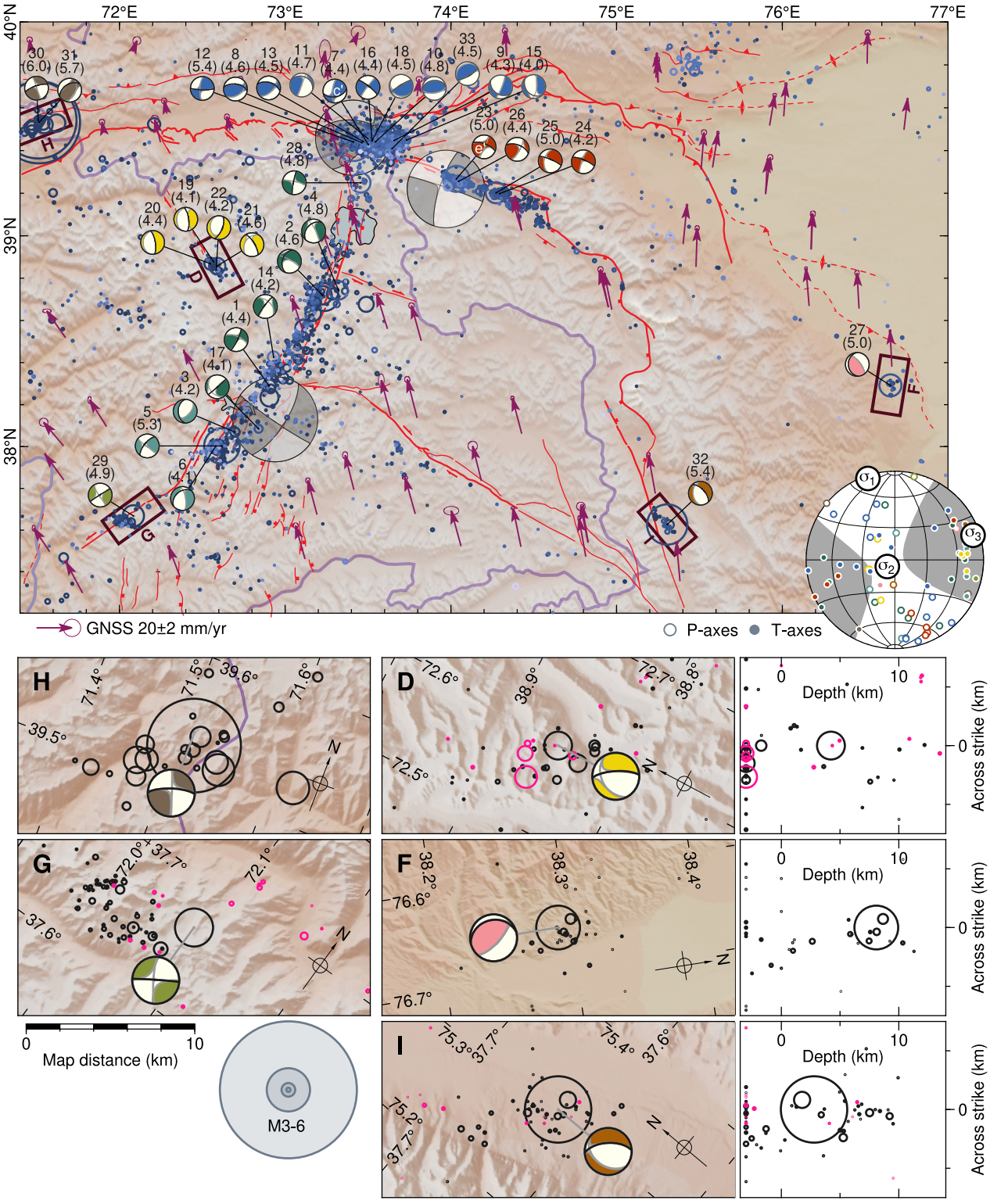
72°E
73°E
74°E
75°E
76°E
77°E
40°N
39°N
38°N
GNSS 20±2 mm/yr
P-axes
T-axes
H
D
G
F
I
Depth (km)
Across strike (km)
Map distance (km)
M3-6

**Figure 8.** Summary of moment tensor results. Moment tensors colored by earthquake sequence as in Figure 3 and numbered as in Table 1. $M_W$ given in parenthesis. Interpreted fault planes are marked in the beach balls in black; fault planes preferred by stress inversion are marked in the beach balls in dark gray; auxiliary plane in light gray. Top: regional overview map. GNSS vectors from Zubovich et al. (2010) and Ischuk et al. (2013). Major neotectonic faults in red. Bottom: close-ups for sequences framed in the top subfigure; foreshocks (magenta); main- and aftershocks (black). (H, G) map views. (D, F, I) with additional across-strike profiles. Inset: stereographic projection of moment- and stress tensor principal axes. Positive areas of the stress tensor are shaded. Lower hemisphere stereographic projection.